On how thin submarine flows transported large volumes of sand for hundreds of kilometres across a flat basin plain without eroding the sea floor

CHRISTOPHER J. STEVENSON*, PETER J. TALLING†, ESTHER J. SUMNER‡, DOUGLAS G. MASSON†, MICHEAL FRENZ§ and RUSSELL B. WYNN†
*Earth and Environment, University of Leeds, Leeds LS2 9JT, UK (E-mail: C.J.Stevenson@leeds.ac.uk)
†Marine Geoscience, National Oceanography Centre Southampton, European Way, Southampton, SO14 3ZH, UK
‡Ocean and Earth Science, University of Southampton, Southampton, UK
§Micrometrics GmbH, Rutherford 108, Aachen 52072, Germany

ABSTRACT

Submarine gravity currents, especially long run-out flows that reach the deep ocean, are exceptionally difficult to monitor in action, hence there is a need to reconstruct how these flows behave from their deposits. This study mapped five individual flow deposits (beds) across the Agadir Basin, offshore north-west Africa. This is the only data set where bed shape, internal distribution of lithofacies, changes in grain size and sea floor gradient, bed volumes, flow thickness and depth of erosion into underlying hemipelagic mud are known for individual beds. Some flows were 30 to 120 m thick. However, flows with the highest fraction of sand were less than 5 to 14 m thick. Sand was most likely to be carried in the lower 5 to 7 m of these flows. Despite being relatively thin, one flow was capable of transporting very large volumes of sediment (*ca* 200 km^3) for large distances across very flat sea floor. These observations show that these relatively thin flows could travel quickly enough on very low gradients (0·02° to 0·05°) to suspend sand several metres to tens of metres above the sea floor, and maintain those speeds for up to 250 km across the basin. Near uniform hemipelagic mud interval thickness between beds, and coccolith assemblages in the mud caps of beds, suggest that the flows did not erode significantly into the underlying sea floor mud. Simple calculations imply that some flows, especially in the proximal part of the basin, were powerful enough to have eroded hemipelagic mud if it was exposed to the flow. This suggests that the flows were depositional from the moment they arrived at a basin plain location, and that deposition shielded the underlying hemipelagic mud from erosion. Reproducing the field observations outlined in this exceptionally detailed field data set is a challenge for future experimental and numerical models.

Keywords Deep water, flow thickness, long run-out, mud erosion, quantitative flow reconstruction, turbidity current flow processes.

INTRODUCTION

Submarine sediment density flows (herein abbreviated to 'submarine flows') include a range of flow types from turbidity current to debris flow (Talling *et al.*, 2012). These flows are the main process for transporting large volumes of sediment from the continental shelf to

the deep ocean, and in some cases they are able to run-out for hundreds to several thousand kilometres (Piper *et al.*, 1999; Wynn *et al.*, 2002b, 2010; Sumner *et al.*, 2012). It is also important to understand turbidity currents because they pose a significant geohazard to sea floor infrastructure, such as oil and gas pipelines (Zakeri, 2008) and communication cables (Heezen *et al.*, 1964; Krause *et al.*, 1970; Piper *et al.*, 1999; Hsu *et al.*, 2008; Carter *et al.*, 2012), upon which modern society is increasingly reliant. Ancient deposits from submarine flows can contain economically important hydrocarbon reserves with many producing fields around the world (Stow & Mayall, 2000).

Current understanding of the dynamics of natural submarine flows is hampered by a paucity of direct measurements, especially for longer run-out flows that reach the deep ocean. The velocity of such long run-out flows has been measured in just five locations worldwide (Talling *et al.*, 2014), mainly from sea floor cable breaks, (Prior *et al.*, 1987; Zeng *et al.*, 1991; Khripounoff *et al.*, 2003; Xu *et al.*, 2004; Vangriesheim *et al.*, 2009; Cattaneo *et al.*, 2012). Flow thickness has been documented directly by moored sensors in just two deep water (>2000 m) locations (Khripounoff *et al.*, 2003; Vangriesheim *et al.*, 2009; Khripounoff *et al.*, 2012; Cooper *et al.*, 2013) and the sediment concentration of large flows in the deep ocean has never been measured directly. Therefore, current understanding of long run-out submarine flow dynamics is derived primarily from analysis of their deposits, together with laboratory-scale experiments and numerical simulations.

This contribution is based on an unusually comprehensive field data set in which individual flow deposits have been mapped out across large (>250 km) distances using numerous cores from the modern sea floor. Such long distance mapping of individual deposits is extremely rare and provides key insights into how flows evolve (Amy & Talling, 2006; Talling *et al.*, 2007a,b; Sumner *et al.*, 2012). It is advantageous to use data from modern cores because changes in the sea floor gradient are known, and the size of non-cemented grains can be measured easily. The Agadir Basin, offshore NW Africa, currently provides the only location where large-scale single bed geometry can be compared to detailed information on deposit grain sizes and changes in sea floor gradient (Talling *et al.*, 2007b; Sumner *et al.*, 2012; Stevenson *et al.*, 2013). Previous work has shown that these flows eroded

little underlying hemipelagic mud (Weaver & Thomson, 1993; Weaver, 1994; Wynn *et al.*, 2002b) and have qualitatively inferred flow evolution from deposit geometries (Talling *et al.*, 2007b; Sumner *et al.*, 2012). The present study also constrains flow thickness using the heights to which deposits drape up basin margins. This provides the first large-scale field data set for long run-out turbidity currents that includes detailed information on bed geometry and grain sizes, flow thickness, sedimentary structures and facies, depth of erosion into underlying hemipelagic mud, and changes in sea floor gradient.

After qualitatively inferring flow evolution from bed geometries, this contribution explores the degree to which the field data can place quantitative constraints on key flow parameters, such as flow speed (U) and bed shear velocity ($U*_f$). Few studies have attempted to reconstruct quantitative flow parameters from deposits (Komar, 1969, 1973; van Tassell, 1981; Bowen *et al.*, 1984; Komar, 1985; Reynolds, 1987; Pirmez & Imran, 2003; Migeon *et al.*, 2012; Sequeiros, 2012), and even fewer studies have done this for long run-out flows that reach beyond the continental slope (Bowen *et al.*, 1984; Reynolds, 1987). Here, three independent approaches are used to estimate flow speeds and bed shear stress based on: (i) the bed shear velocity necessary to suspend grains of a certain size; (ii) the downslope component of the gravitational force for flows of known thickness and variable density; and (iii) the flow speeds and bed shear velocities necessary to erode hemipelagic mud, assuming that this mud is exposed below the flow. The assumptions behind each of these three approaches are discussed, and the results that are presented include a range of feasible values for empirical parameters. It will be difficult to collect field data sets that are more complete for individual deposits. It is therefore important to understand what this data set can reveal about long run-out submarine flows that reach the deep ocean, and it is hoped that future authors will compare more sophisticated models to this field data set.

Aims

This paper presents an exceptionally detailed field data set, which documents five individual beds across the Agadir Basin, offshore NW Africa (Fig. 1). The first aim was to constrain flow thicknesses using the heights to which flow

deposits drape up basin margins, and to discuss the assumptions that underlie such estimates. The second aim was to understand flow evolution qualitatively using sedimentary facies and bed geometries. The third aim was to assess the degree to which quantitative estimates of key flow parameters can further constrain the evolving character of these flows.

Study area: The Agadir Basin

The Agadir Basin is one of three interconnected basins that make up the Moroccan Turbidite System, situated offshore NW Africa (Fig. 1A and B). Over the past 200 kyr, this system has been host to a series of large volume (some >100 km^3) turbidity currents that have exceptionally long run-out distances (Wynn *et al.*, 2002b; Talling *et al.*, 2007b; Wynn *et al.*, 2010; Stevenson *et al.*, 2013). The Agadir Basin covers an area *ca* 35 000 km^2 and occupies water depths of between 4300 m and 4500 m. The basin slopes towards the south-west and comprises two particularly flat areas (<0·01°) separated by a slightly steeper ramp (*ca* 0·03°; Fig. 1C). Its southern margin opens out onto the continental rise, marked by an increase in slope from *ca* 0·02° to 0·06° (Wynn *et al.*, 2012; Stevenson *et al.*, 2013). Flows enter the system from three sources: volcanoclastic flows from the Canary Islands; siliciclastic flows from the Moroccan Margin; and carbonate-rich flows sourced from localized seamount collapses (Rothwell *et al.*, 1992; Weaver *et al.*, 1992; Wynn *et al.*, 2002b). Deposits indicate that many of these flows were 120 to 150 km wide, extending across the entire width of the Agadir Basin.

Previous work has established a robust geochemical, biological and chronostratigraphic framework allowing individual beds to be correlated across all three sub-basins (Weaver & Kuijpers, 1983; Weaver, 1991; Rothwell *et al.*, 1992; Weaver *et al.*, 1992; Weaver & Thomson, 1993; Weaver, 1994; Davies *et al.*, 1997; Wynn *et al.*, 2002b; Talling *et al.*, 2007b; Wynn *et al.*, 2010). In the present study, bed correlations are presented as online supplementary material (Figs S1 to S3; see also Frenz *et al.*, 2008). Beds A3, A5, A7, A11 and A12 are the focus of this study. These five beds were chosen because they have similar siliciclastic sand fraction mineralogy compositions, with smectite and illite comprising between 60% and 80% of the clay mineralogy (Pearce & Jarvis, 1992), and flow pathways from the Moroccan Margin to the

Agadir Canyon. The flows all spread across the Agadir Basin from north-east to south-west (Wynn *et al.*, 2002a,b; Frenz *et al.*, 2008).

METHODS

### Sea floor bathymetry and slope

GEneral Bathymetric Chart of the Oceans (GEBCO) data are used to generate slope maps across the Agadir Basin. Sea floor gradients are calculated from spot depths, which are then smoothed (averaged) within a 3 km^2 grid (see http://www.gebco.net/data_and_products/gridded_bathymetry_data for details). There is good agreement between sea floor gradients calculated from GEBCO data and sea floor gradients calculated between core sites using trigonometry. To assess the impact of spatially variable submarine flow deposition on sea floor bathymetry over the past 200 kyr, individual beds were sequentially removed from the stratigraphy and the resulting palaeobathymetry calculated (Fig. S4). This analysis suggests that palaeobathymetry and sea floor gradients are similar to those observed on the modern sea floor, although differential tectonic subsidence is not included.

Cores and grain-size analysis

The 29 sediment cores used in this study were collected during *RRS Charles Darwin* cruise *CD166* (core locations are shown in Fig. 1B). Cores were recovered using a *ca* 12 m piston corer. The average spacing between cores is *ca* 15 km with each core recovering *ca* 8 m of sediment. Each core was visually logged in detail and flow deposits were analysed for grain size. Grain-size samples were taken approximately every 1 cm vertically through beds. Samples were mixed with 60 ml of 1% deflocculent (sodium hexametaphosphate) solution, and then shaken for at least 10 h to break up any aggregates of sediment. Samples were analysed using laser diffraction by a Malvern Mastersizer 2000 (Malvern Instruments Limited, Malvern, UK). Three grain-size distribution measurements were carried out on each sample from which average particle-size distributions were calculated.

Heights to which beds drape up basin margins
Vertical heights to which deposits drape up basin topography were calculated from the deepest core sites in transects 2 and 3 trending up
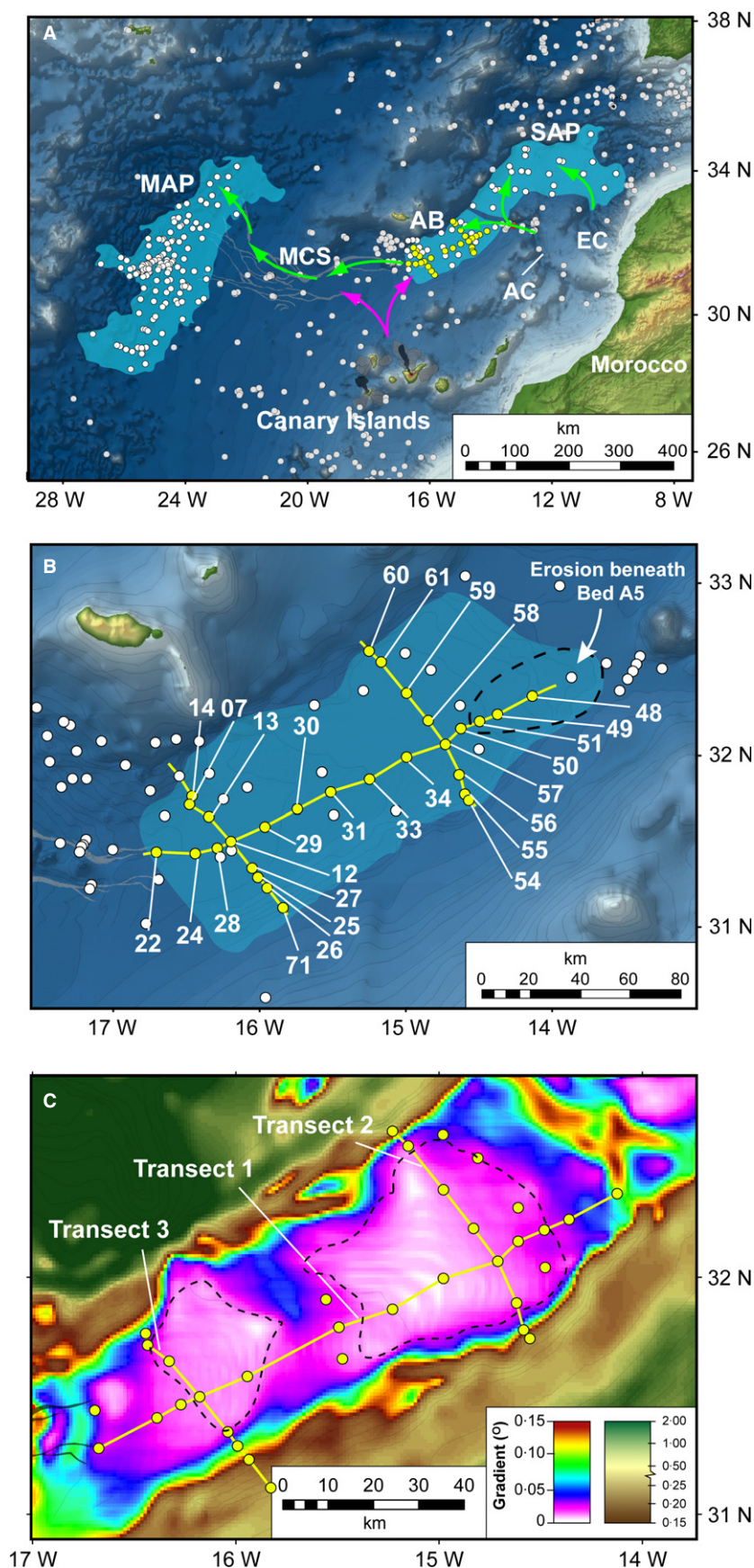
Fig. 1. Map of the Moroccan Turbidite System, offshore NW Africa. (A) Regional map showing the entire Moroccan Turbidite System extending across: the Seine Abyssal Plain (SAP), the Agadir Basin (AB), the Madeira Channel System (MCS) and the Madeira Abyssal Plain (MAP). Feeding the system are a number of canyons, the largest of which are the Agadir and El Jadida Canyons, marked AC and EC, respectively. All cores that have been recovered from the area are shown with white circles. Cores used in this study are highlighted in yellow. Major flow pathways are highlighted for organic-rich flows sourced from the Moroccan Margin (green arrows), and volcanoclastic flows sourced from the Canary Islands (purple arrows). (B) Map of the Agadir Basin showing names and locations of cores used in this study (yellow circles). (C) Slope map of the Agadir Basin. Core transects 1 to 3 are labelled. Note the two flatter areas within the Agadir Basin (*ca* 0·01°) that are separated by a steeper ramp (*ca* 0·03°).

the basin margin (Fig. 1B), which are site 57 (4398 m water depth) and site 13 (4431 m water depth), respectively. For example, site 54 in transect 2 has a water depth of 4374 m, which is 24 m above site 57. A bed that is found in sites 54 and 57 is therefore inferred to drape at least 24 m up the basin margin.

RESULTS

Sedimentary facies

Two distinct types of deposit are found in the cores: (i) background hemipelagic mud; and (ii) submarine flow deposit sand and mud. Hemipelagic sediments comprise two end member lithologies. During interglacial periods, the sediments are cream-coloured carbonate oozes, comprising foraminifera tests, coccolithophores and some fine terrigenous clay (Weaver & Kuijpers, 1983; Weaver & Rothwell, 1987; Rothwell *et al.*, 1992; Weaver *et al.*, 1992). In glacial periods, increased rates of carbonate dissolution in the bottom waters dissolved most of the foraminifera tests and coccolithophores, leaving a smooth dark brown clay (Crowley, 1983; Weaver *et al.*, 1992). Deposits from submarine flows (event beds) are distinguished from hemipelagic sediment via a sharp change in grain size and a distinct change in colour.

Bed facies and bed geometries

Beds A3, A5, A7, A11 and A12 are described succinctly utilizing facies schemes adapted from Sumner *et al.* (2012) and Talling *et al.* (2012) (Table 1). The reader is referred to these papers for a more detailed discussion on the facies outlined in Table 1. Figure 2 provides a key to Figs 3 to 12, which show bed geometries, grain-size profiles, facies distributions and sea floor gradients for across-flow and downflow trending profiles through Beds A3, A5, A7, A11 and A12. Each bed is now briefly described.

Bed A3
The sand deposits of Bed A3 (Figs 3 and 4) do not extend far into the basin (*ca* 50 km) and comprise planar-laminated sands (6 cm thick) overlain by an interval of structureless sand (6 cm thick). Laterally, these sands grade into *ca* 5 cm thick ripple cross-laminated sands (Fig. 4B). A 10 to 30 cm thick mud cap overlying the sands is largely composed of ungraded,

structureless mud with occasional inter-laminated silts and muds at its base (for example, Fig. 4F).

Bed A5
The sand deposits of Bed A5 extend across the entire length (Fig. 5) and breadth (Fig. 6) of the Agadir Basin. In general, deposits comprise 1 to 2 cm thick very coarse-grained lags that have sharp tops, overlain by finer-grained structureless sands often inter-bedded with planar-laminated sands between 20 cm and 30 cm thick. Mud-rich sand intervals (40 to 180 cm thick) are developed across flatter parts of the basin, overlying structureless and planar-laminated sands (Fig. 5B). In cross-section, the mud-rich intervals are shown to be developed within the core of the bed, surrounded by 30 to 50 cm thick structureless and planar-laminated sands (Fig. 6B and C). The basal grain size of deposits is very similar throughout the basin and does not appear to fine downslope (Fig. 5A and C). Overlying the sand facies is a relatively thin silt and mud interval that is 10 to 60 cm thick. In places, the mud cap exhibits subtle contortions and nodules of silt and/or very fine sand (for example, Core 57; Fig. 5B).

Bed A7
The sand deposits of Bed A7 extend across the entire Agadir Basin (Figs 7 and 8); they comprise relatively thin (6 to 15 cm thick) ripple cross-laminated and convoluted sands overlain by thicker (typically between 20 cm and 60 cm) silts and muds. The overlying mud is composed of inter-laminated silts and muds, ungraded structureless muds, and mud intervals with subtle contortions and nodules of silt. Relatively thick (5 to 15 cm) intervals of contorted mud facies occur on the two flatter parts of the Agadir Basin (Fig. 7B) and in cross-section are asymmetrically developed towards the margins of the basin (Fig. 8B and E). The basal sands are uniform in grain size with no particular fining trends (Fig. 7C).

Bed A11
Overall, the sand deposits of Bed A11 extend *ca* 100 km down the Agadir Basin (Fig. 9) and, in proximal areas, cover the entire width of the basin (Fig. 10). Initially, deposits are relatively thick (*ca* 80 cm) comprising structureless and planar-laminated sands (*ca* 55 cm thick), overlain by a 25 cm thick contorted sand interval (for example, Core 48; Fig. 9B). Approximately

Table 1. Summary of facies used in this study. Synonymous facies described in existing facies schemes are listed. For detailed discussion as to the origins of each facies, the reader is referred to Talling *et al.* (2012) and Sumner *et al.* (2012).

Facies	Description	Grain size			Thickness	Grading	Position	Associated facies				Interpretation	Equivalent facies
								Vertical		Lateral			
		Range (μm)	Mode (μm)	Sorting	Range (cm)			Above	Below	Upstream	Downstream		
Clean structureless sand (lower and upper)													
ST_B	Clean sand with no sedimentary structures	82 to 200	*ca* 600	1·5 to 2·5	10 to 63	Mostly ungraded. Normal and inverse	Proximal, Basal parts of deposit	PL CL ST_D M	PL	ST_B PL	PL	Rapid deposition from a high-density turbidity current (Lowe, 1982; Kneller & Branney, 1995; Sumner *et al.*, 2008)	T_A (Bouma, 1962) S_3 (Lowe, 1982)
ST_U	Clean sand with no sedimentary structures	44 to 72	*ca* 177	1·5 to 2	6 to 13	Weak normal grading, multiple grading sequences	Distal, Upper parts of deposit	PL RXL M	PL LXL CL RXL	CL LXL	LXL RXL	Capacity-induced collapse of sediment from the rear part of a turbidity current	N/A
Mud-rich structureless sand													
ST_D	Mud-rich (30 to 40%) structureless sand, mud clasts can be present (See Talling *et al.*, 2007b	72 to 320	*ca* 250	2·4 to 3	5 to 138	Weak normal grading proximal. Ungraded distal	Proximal, central parts of deposit. Distal progressively higher in deposit	GSB M	ST_B PL	ST_U PL	PL	*En masse* deposition from a mud-rich debris flow developed towards the rear of a turbidity current (Talling *et al.*, 2007b)	H_3 (Haughton *et al.*, 2009)
Planar-laminated sand													
PL	Clean sand with parallel lamination, most common deposit type	62 to 250	*ca* 250	*ca* 1	5 to 58	Proximal, inverse to normal grading. Distal, weak normal grading	Middle and lower parts of deposit	GSB LXL ST_D M	ST_B ST_U (Rarely)	ST_B CL ST_D	LXL RXL ST_D	1. Collapsing laminar sheared layers at the base of a high-density turbidity current (Vrolijik & Southard, 1997; Sumner *et al.*, 2008) 2. Migration of low amplitude bedwaves along the base of a dilute flow (Allen, 1982; Best & Bridge, 1992)	T_B (Bouma, 1962) H_4 (Haughton *et al.*, 2009)

Table 1. (continued)

Facies	Description	Grain size		Sorting	Thickness	Grading	Position	Associated facies				Interpretation	Equivalent facies
		Range (μm)	Mode (μm)		Range (cm)			Vertical		Lateral			
								Above	Below	Upstream	Downstream		
Low-angle cross-laminated sand													
XL	Clean sand with low-angle (<10°), non-parallel lamination	177 to 350	*ca* 200	*ca* 1	5 to 20	Inverse and normal grading	Middle and upper parts of deposit	GSB RXL ST_U	PL	PL	RXL CL	1. Amplification of perturbations caused by boundary layer instabilities (Arnott, 2012) 2. Tractional reworking of sediment with mud effecting near-bed flow field (Baas *et al.*, 2011; Sumner *et al.*, 2012)	T_{B-C} (Bouma, 1962)
Ripple cross-laminated sand													
RXL	Clean sand with high angle (>10°) cross-lamination. Laminae often truncated	62 to 190	*ca* 150	0.6 to 1	5 to 13	Normal grading. Rare inverse grading	Distal, upper parts of deposit	ST_U CL GSB M	LXL	CL LXL PL	CL	Tractional reworking of sediment along the bed from a dilute, decelerating turbidity current (Allen, 1982)	T_C (Bouma, 1962) H_4 (Haughton *et al.*, 2009)
Convolute/contorted laminated sand													
CL	Sand with contorted laminations	110 to 350	*ca* 150	1 to 2.3	7 to 45	Normal grading	Proximal and distal. Middle and upper parts of deposit	ST_U GSB M	RXL LXL ST_B	RXL	PL RXL	Excess pore pressure re-suspends sediment resulting in contortion of existing sedimentary structures (Allen, 1977)	T_C (Bouma, 1962)
Laminated silt and mud													
L	Fine-grained mud with silt laminations	15 to 62	*ca* 20	1.2 to 1.4	3 to 21	Normal grading	Upper parts of deposit. Basal parts of mud cap	GSB CM M	ST_U PL RXL	CM M	M	Alternating near-bed boundary conditions from granular to cohesive, within a dilute decelerating turbidity current (Piper, 1972, 1978; Stow & Bowen, 1978, 1980)	T_D (Bouma, 1962) T_{2-3} (Stow & Shanmugam, 1980) E_1 (Piper, 1978)

(continued)

Table 1. (continued)

Facies	Description	Grain size Range (μm)	Mode (μm)	Sorting	Thickness Range (cm)	Grading	Position	Associated facies Vertical Above	Below	Lateral Upstream	Downstream	Interpretation	Equivalent facies
Contorted mud													
CM	Fine-grained mud matrix with contorted silt laminations and silt/sand clasts	10 to 70	*ca* 20	1·8 to 3	5 to 23	Ungraded. Rare weak normal grading	Upper parts of deposits. Middle and lower parts of mud cap	M	GSB L M PL ST$_U$	L M	L M	1. Collapse of muddy suspension, in the tail end of a dilute turbidity current, into a cohesive fluid mud layer (Kneller & McCaffrey, 2003; Talling *et al.*, 2007) 2. Remobilization of mud off nearby slopes	T$_{4-6}$ (Stow & Shanmugam, 1980)
Mud													
M	Fine-grained structureless mud	2 to 32	*ca* 18	1·5 to 3	8 to 44	Ungraded. Some normal grading at base	Upper parts of deposit	CM	GSB CM LXL RXL ST$_U$	L CM	L CM	1. Slow settling of fine silt and hydraulically equivalent clay flocs from a dilute turbidity current 2. Cohesive fluid mud layer develops near to bed and freezes '*en masse*' (McCave & Jones, 1988)	T$_E$ (Bouma, 1962) E$_3$ (Piper, 1978) T$_{7-8}$ (Stow & Shanmugam, 1980)

Grain size (µm)		Sedimentary structures			
		Graphic	Label	Colour	Description
▬ (blue)	D90	(dotted graphic)	ST	(green)	Structureless gravel sized particles, often with shell fragments
▬ (red)	D50		ST	(green)	Clean and structureless
▲ (green)	D10		ST	(purple)	Mud-rich and structureless
● (black)	Sorting (*after Folk & Ward, 1957*)	(graphic)	ST$_D$	(purple)	Mud-rich with clasts
Symbols		(horizontal lines)	PL	(red)	Parallel lamination
(red triangle left)	Grain-size break overlain with finer sediment	(low-angle lines)	LXL	(dark blue)	Low-angle cross-lamination
(red triangle left)	Grain-size break overlain with coarser sediment	(ripple graphic)	RXL	(yellow)	Ripple cross-lamination
(red wavy)	Sharp and/or erosive boundary	(contorted graphic)	CL	(orange)	Contorted lamination
(grey box)	Turbidite sediment	(lines)	L	(brown)	Mud/silt lamination
(dotted box)	Hemipelagic mud	(contorted mud graphic)	CM	(magenta)	Contorted mud
X	Turbidite pinch-out		M	(light blue)	Structureless mud

Fig. 2. Key to all figures using graphic logs. Figure includes: symbology for graphic logs and vertical grain-size profiles, and colours and abbreviations for interpreted facies.

25 km downslope (between Cores 48 and 49), Bed A11 thins dramatically with deposits of parallel-laminated sands reaching only 8 to 15 cm in thickness. Down the axis of the basin, these parallel-laminated sands maintain their thickness and extend a further *ca* 75 km downslope. Across the width of the basin, parallel-laminated sands grade into ripple cross-laminated and contorted sands of similar thicknesses (Fig. 10B). Coarse-tail grading is seen in the grain size of the basal sands downslope (Fig. 9C). The mud cap overlying the sands is initially thin (10 cm) and progressively thickens to *ca* 30 cm at the distal end of the Agadir Basin (Fig. 9). The mud is generally ungraded and structureless, but can have normally graded intervals of inter-laminated silts and muds at its base (for example, Core 12; Fig. 9B).

Bed A12
Sand deposits of Bed A12 extend across the entire Agadir Basin and maintain a similar thickness throughout (Figs 11 and 12). In proximal parts of the basin, the bed comprises 5 to 15 cm thick ungraded structureless sands, overlain by 10 to 35 cm thick parallel-laminated sands.

Occasionally, the structureless sands show inverse grading at their base (for example, Core 51; Fig. 11A). Laterally, structureless and parallel-laminated sands grade into ripple cross-laminated sands (Fig. 12B). Approximately 150 km downslope, structureless and parallel-laminated sands thin and grade into low-angle and ripple cross-laminated sands 30 to 40 cm thick. The basal sands have a coarse-tail grading for the first 100 km along the basin before becoming relatively uniform downslope (Fig. 11C).

Erosion beneath beds

At least some of these flows were partly or wholly responsible for localized erosion around the mouth of the Agadir Canyon, which produced a scour field with deep (>20 m) and extensive (5 km long) scours (Fig. 1B) (Wynn *et al.*, 2002a; Macdonald *et al.*, 2011). Erosion to a depth of *ca* 1 m beneath Bed A5 occurs within one core (no. 57) in the most proximal part of the Agadir Basin (Figs 1B and S1). However, bed correlations across the rest of the Agadir Basin show that there is no significant differential (>1 to 2 cm) erosion beneath the five beds studied here. Hemipelagic
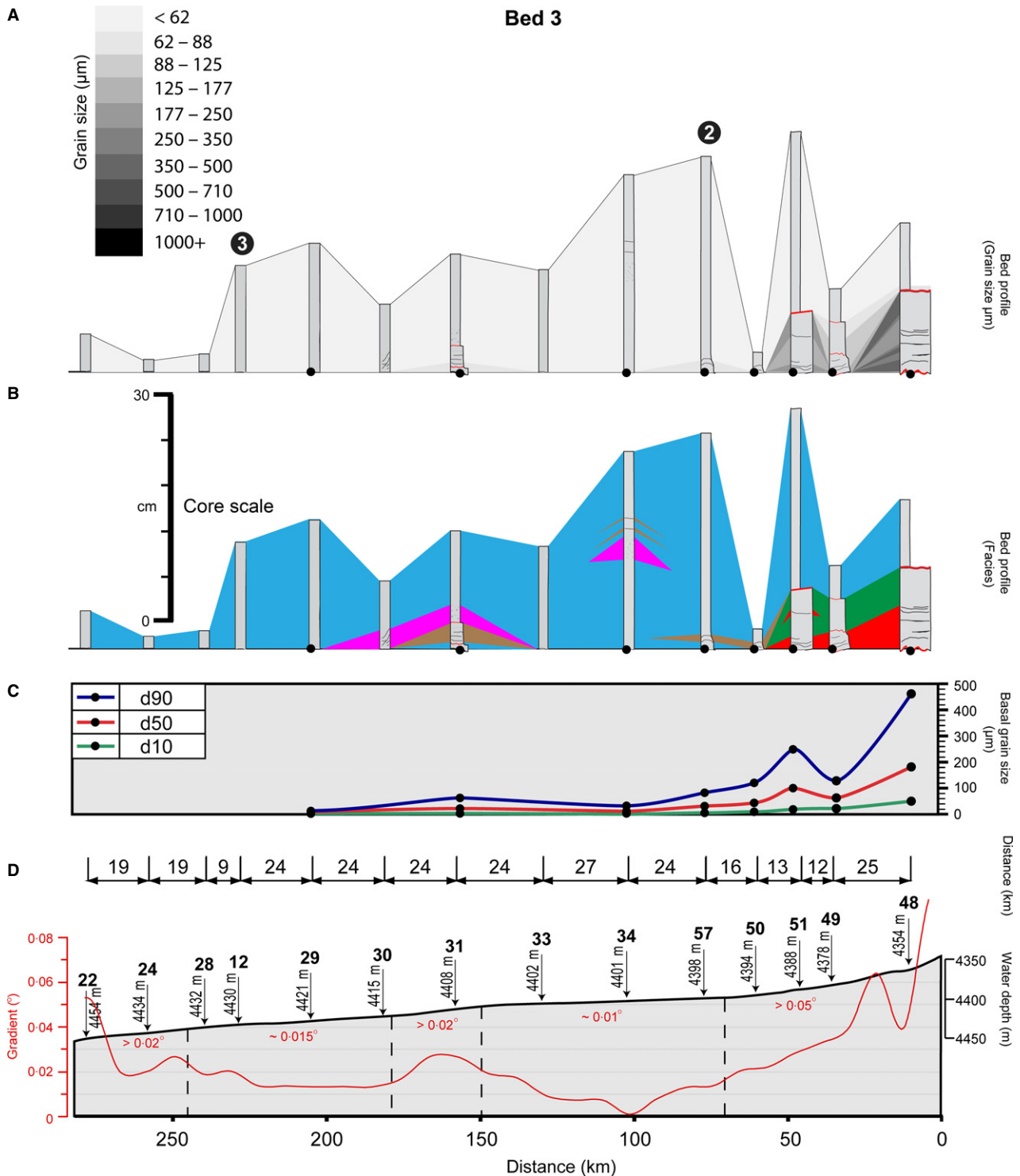
Fig. 3. Bed A3 transect 1 along the axis of the Agadir Basin. Graphic logs are anchored onto a horizontal surface to highlight changes in bed thickness. Refer to Fig. 2 for key. (A) Vertical and spatial distribution of grain size. Positions of across-flow transects 2 and 3 are marked. (B) Colour denotes interpreted facies. (C) Basal grain size at each core site. (D) Sea floor topography (grey shaded area) overlain with sea floor gradient (red line) along the axis of the Agadir Basin.
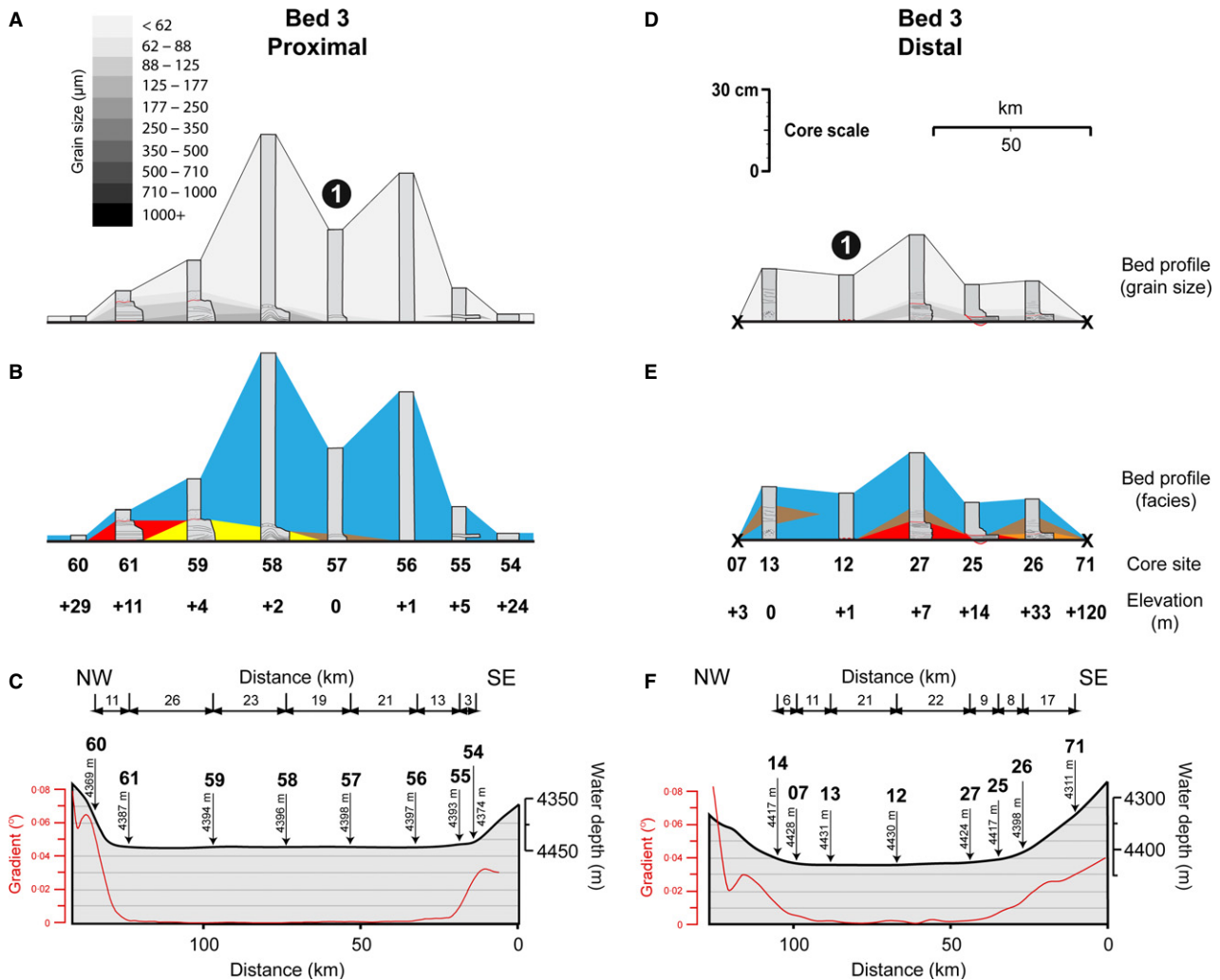
Fig. 4. Bed A3 transects 2 (proximal) and 3 (Distal) from NW to SE across the Agadir Basin. Graphic logs are anchored onto a horizontal surface to highlight changes in bed thickness. (A) and (D) Vertical and spatial distribution of grain size. Position of transect 1 is marked. (B) and (E) Colour denotes interpreted facies. (C) and (F) Sea floor topography (grey shaded area) overlain by sea floor gradient (red line). Vertical exaggeration *ca* 160 times.

intervals that underlie the beds are relatively uniform in thickness and have lithological marker horizons (5 to 10 cm thick glacial clay layers) that can be traced throughout the Agadir Basin (Figs S1 to S3) and across the rest of the Moroccan Turbidite System (Weaver & Kuijpers, 1983; Wynn *et al.*, 2002b; Stevenson *et al.*, 2013). It is possible that flows uniformly eroded down to only a relatively small depth (i.e. 1 or 2 cm), perhaps removing very low density (soupy) mud from just below the sea floor. However, if such a soupy mud layer was <10 cm thick across the (250 km by 100 km) basin floor, and had a volume concentration of <10%, it would only supply <0·25 km³ of mud to the flows. Such erosion could not be identified from missing

lithological horizons or discrete changes in hemipelagic thicknesses across the basin. Coccolith assemblages have been measured within the mud caps of the beds across the basin. Spatially, each bed has similar coccolith assemblages across the basin within its mud cap, which indicates that little erosion occurred along the basin plain (Weaver & Thomson, 1993; Weaver, 1994; Wynn *et al.*, 2002b).

Height to which deposits drape up topography

Lateral patterns of deposition, and the height to which different facies and grain sizes drape up the basin margins, are established using

Fig. 5. Bed A5 transect 1 along the axis of the Agadir Basin. Graphic logs are anchored onto a horizontal surface to highlight changes in bed thickness. Refer to Fig. 2 for key. (A) Vertical and spatial distribution of grain size. Positions of across-flow transects 2 and 3 are marked. (B) Colour denotes interpreted facies. (C) Basal grain size at each core site. (D) Sea floor topography (grey shaded area) overlain with sea floor gradient (red line) along the axis of the Agadir Basin.

Fig. 6. Bed A5 transects 2 (Proximal) and 3 (Distal) from NW to SE across the Agadir Basin. Graphic logs are anchored onto a horizontal surface to highlight changes in bed thickness. (A) and (D) Vertical and spatial distribution of grain size. Position of transect 1 is marked. (B) and (E) Colour denotes interpreted facies. (C) and (F) Sea floor topography (grey shaded area) overlain by sea floor gradient (red line). Vertical exaggeration *ca* 160 times.
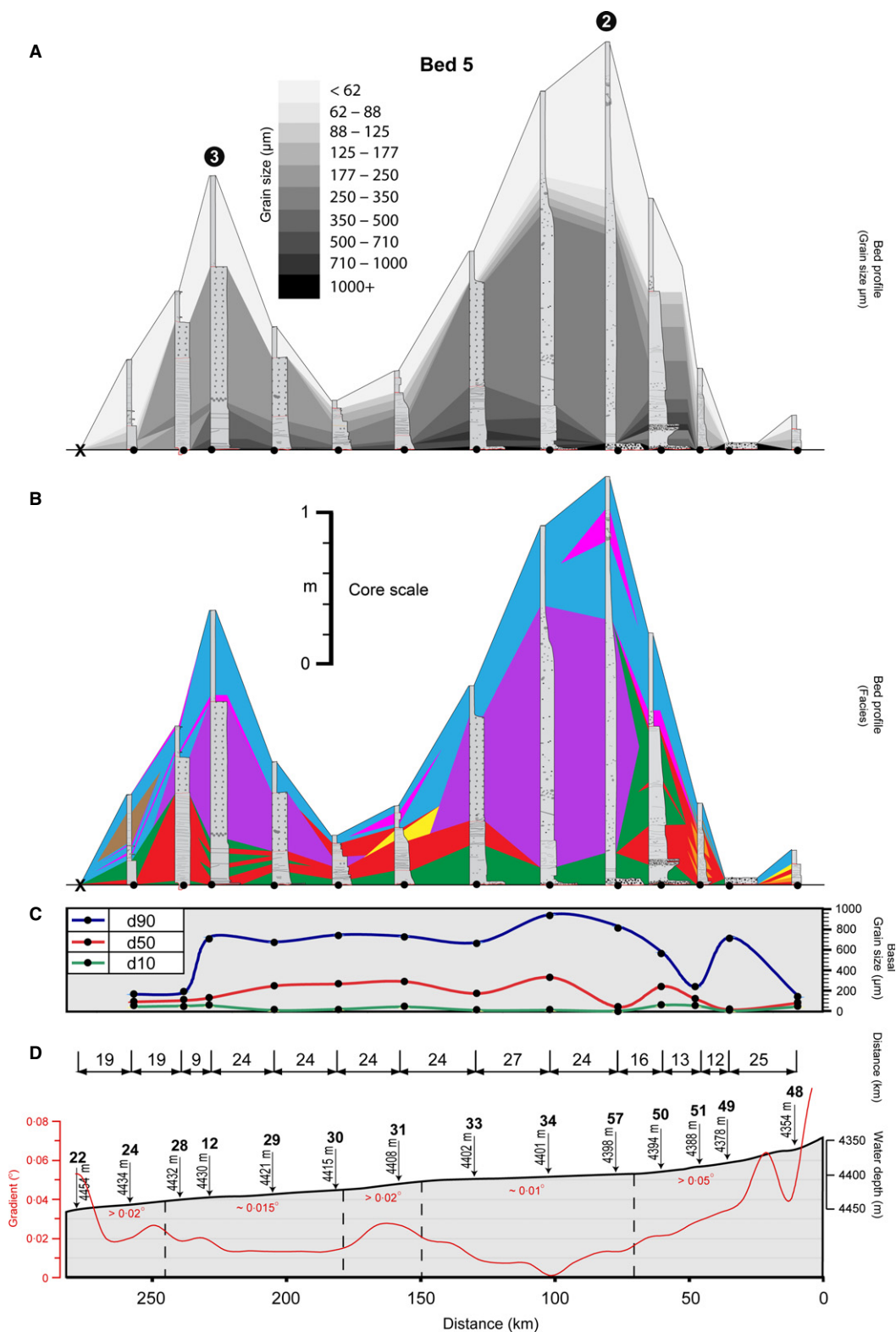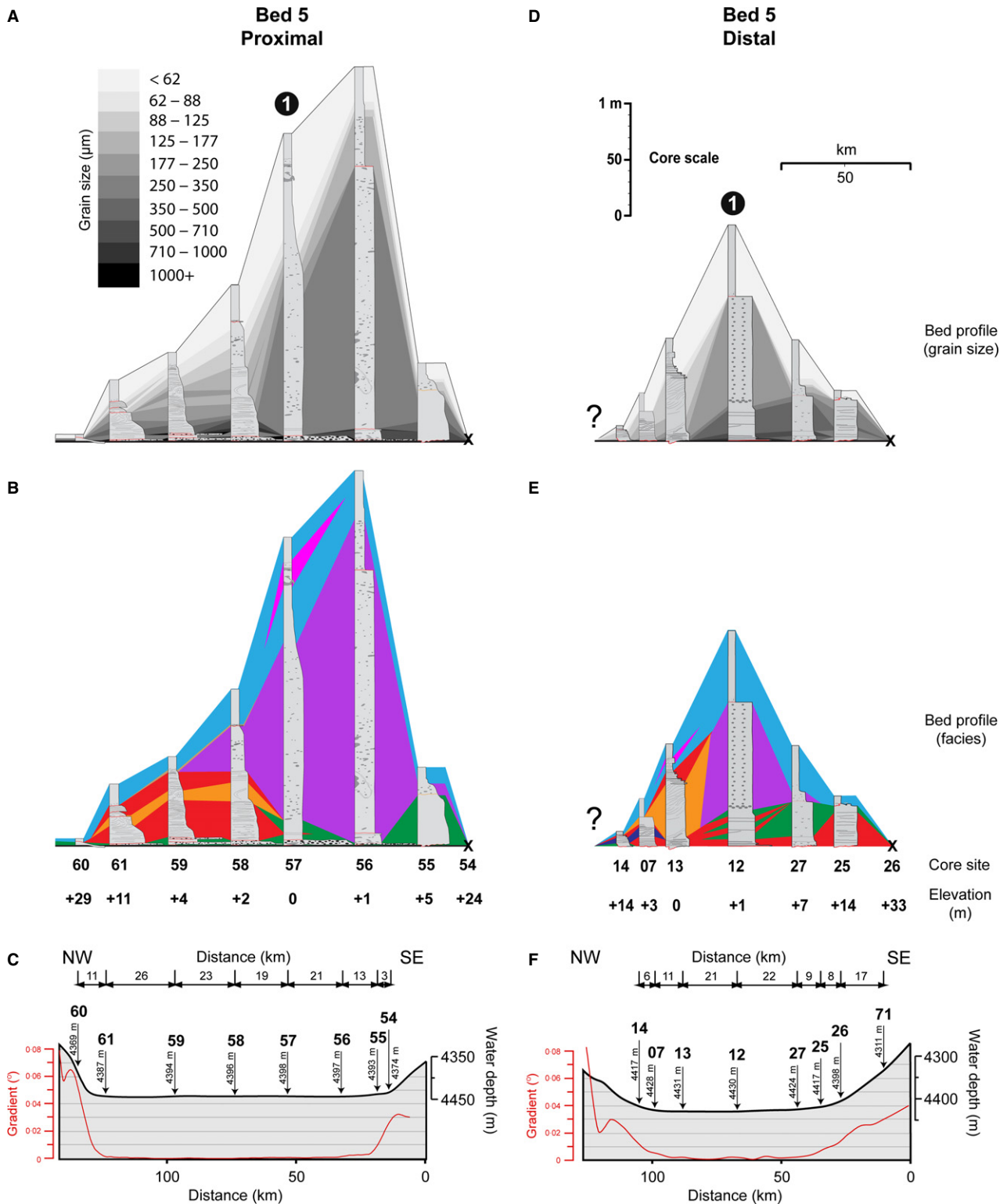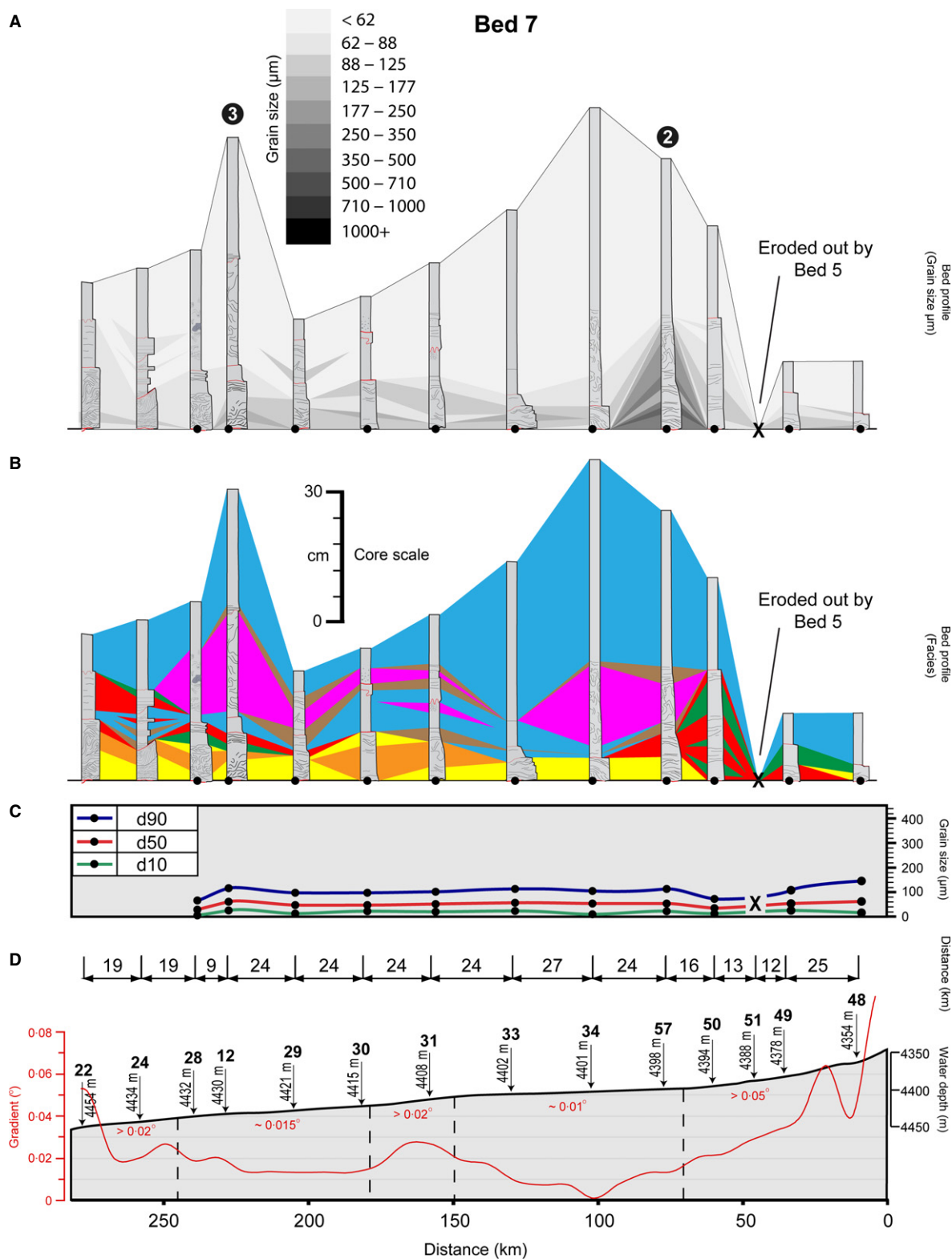
Fig. 7. Bed A7 transect 1 along the axis of the Agadir Basin. Graphic logs are anchored onto a horizontal surface to highlight changes in bed thickness. Refer to Fig. 2 for key. (A) Vertical and spatial distribution of grain size. Position of across-flow transects 2 and 3 are marked. (B) Colour denotes interpreted facies. (C) Basal grain size at each core site. (D) Sea floor topography (grey shaded area) overlain with sea floor gradient (red line) along the axis of the Agadir Basin.

Fig. 8. Bed A7 transects 2 (Proximal) and 3 (Distal) from NW to SE across the Agadir Basin. Graphic logs are anchored onto a horizontal surface to highlight changes in bed thickness. (A) and (D) Vertical and spatial distribution of grain size. Position of transect 1 is marked. (B) and (E) Colour denotes interpreted facies. (C) and (F) Sea floor topography (grey shaded area) overlain by sea floor gradient (red line). Vertical exaggeration *ca* 160 times.

across-flow transects 2 and 3 (Figs S2 and S3) and are summarized in Tables 2 and 3. The complete thickness of the oldest and deepest deposit in this study (Bed A12) was not always recovered. This limits description of the basal part of Bed A12 in across-flow directions.

In the distal transect, Beds A11 and A12 have sandy deposits that pinch out at heights of <5 m above the basin floor, and mud that pinches out at heights of <14 m above the basin floor (Figs 10 and 12; Table 2). Bed A5 extends further up the basin margins with sand and mud layers
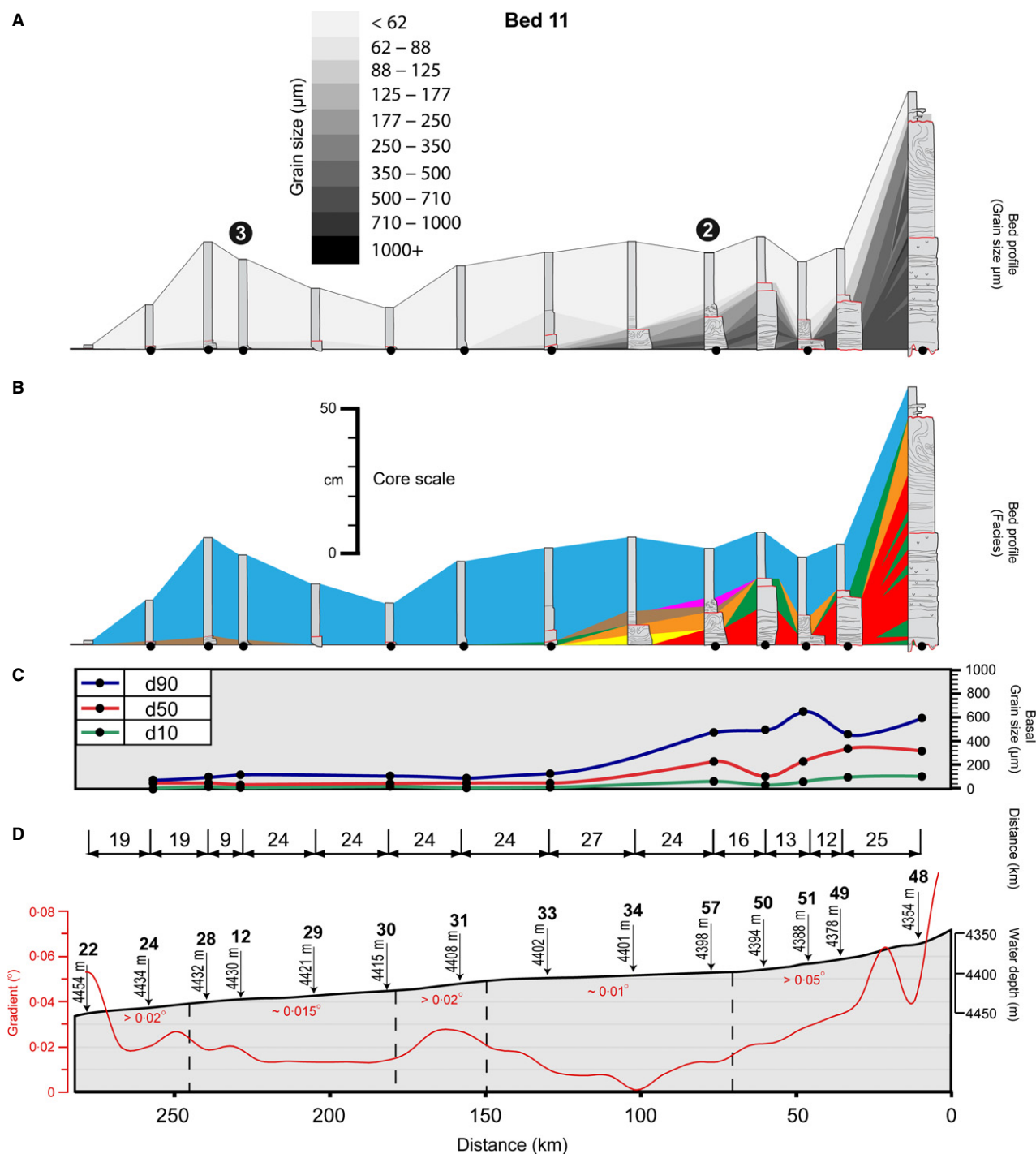
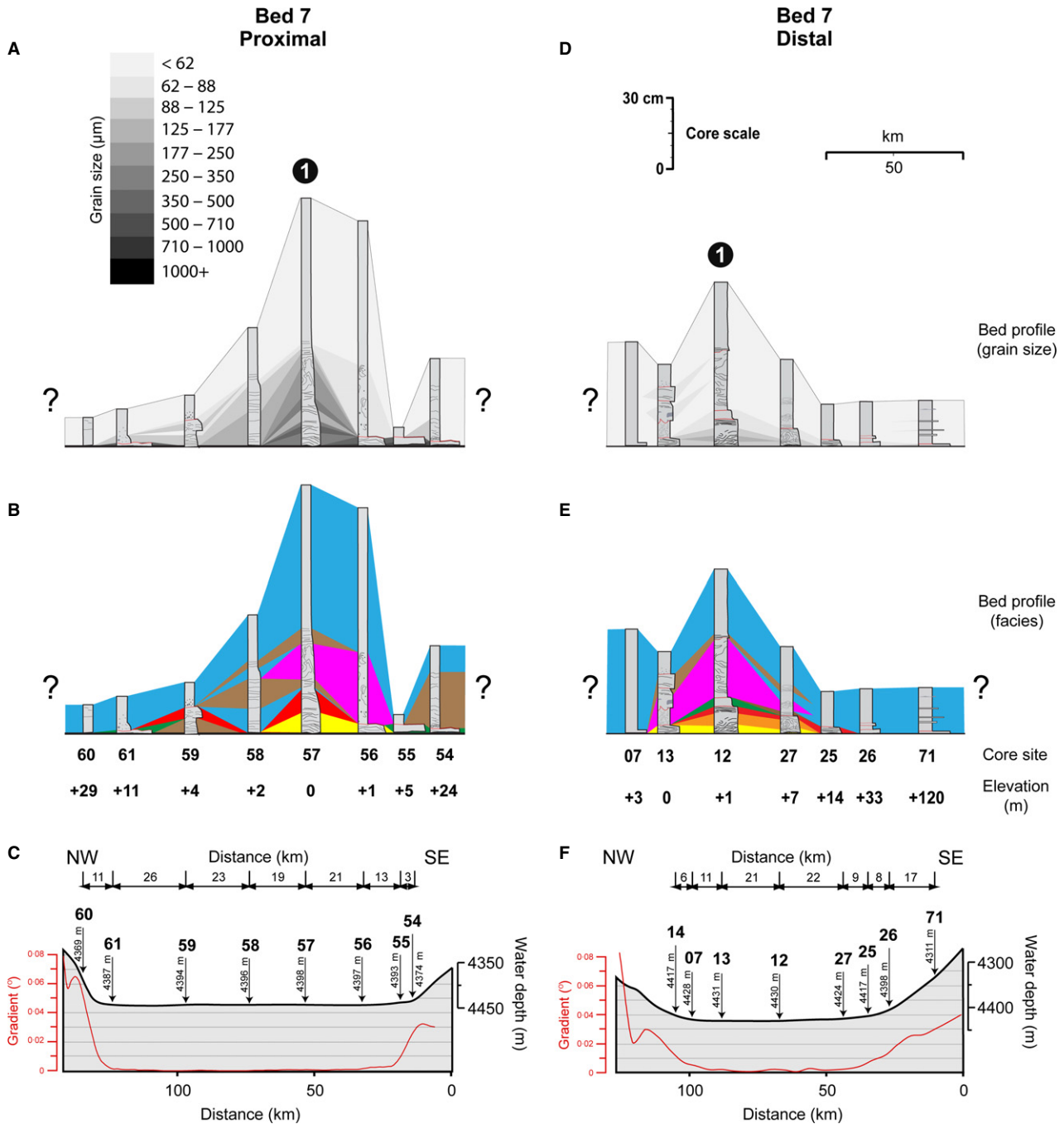**Fig. 9.** Bed A11 transect 1 along the axis of the Agadir Basin. Graphic logs are anchored onto a horizontal surface to highlight changes in bed thickness. Refer to Fig. 2 for key. (A) Vertical and spatial distribution of grain size. Positions of across-flow transects 2 and 3 are marked. (B) Colour denotes interpreted facies. (C) Basal grain size at each core site. (D) Sea floor topography (grey shaded area) overlain with sea floor gradient (red line) along the axis of the Agadir Basin.

extending to heights of less than 24 m above the basin floor (Fig. 6; Tables 2 and 3). In contrast, Beds A3 and A7 both have sand and mud depos-

its that extend much further up the basin margins (>33 m to >120 m), beyond the coverage of the cores (Figs 4 and 8; Tables 2 and 3).

Fig. 10. Bed A11 transect 2 (proximal) from NW to SE across the Agadir Basin. Graphic logs are anchored onto a horizontal surface to highlight changes in bed thickness. (A) Vertical and spatial distribution of grain size. Position of transect 1 is marked. (B) Colour denotes interpreted facies. (C) Sea floor topography (grey shaded area) overlain by sea floor gradient (red line). Vertical exaggeration *ca* 160 times.

Identifying traces of deposition from turbidity currents

Core sites 25, 26, 54 and 55 are located along the margins of the Agadir Basin (Fig. 1B). Upon visual inspection, these core sites do not appear to contain deposits of specific beds and therefore are probably the closest cores above the pinch out of individual beds. It is possible that if the beds were very thin, fine-grained and bioturbated in these locations, then they would be difficult to recognize using visual inspection alone. As a result, detailed grain-size analyses were conducted on these cores to inspect them for cryptic evidence of the beds (Fig. 13).

Hemipelagic carbonate ooze (from interglacial periods) has a bimodal grain-size distribution with modes of *ca* 5 μm and 250 μm, representing clay and foraminifera tests, respectively (Fig. 13C; modes A and C). In glacial periods, the tests are dissolved leaving just the fine clay mode (*ca* 5 μm). Both interglacial and glacial hemipelagic sediments have grain-size distributions with a low frequency of grain sizes between *ca* 35 μm and 70 μm (Fig. 13C; mode B). Traces of sediment from flow deposits will change the signature of the hemipelagic grain-size distribution. Traces of very fine silt/mud (*ca* 20 μm) will either significantly
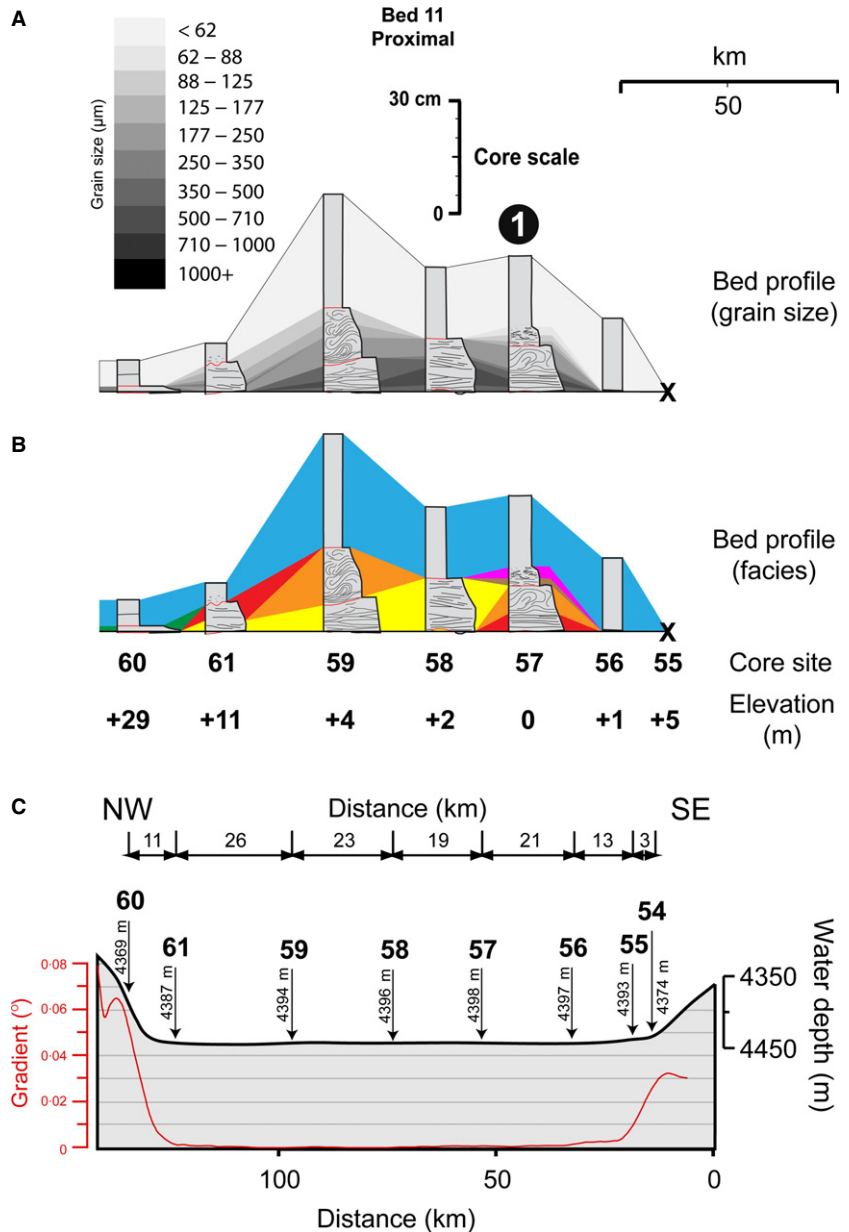
Fig. 11. Bed A12 transect 1 along the axis of the Agadir Basin. Graphic logs are anchored onto a horizontal surface to highlight changes in bed thickness. Refer to Fig. 2 for key. (A) Vertical and spatial distribution of grain size. Positions of across-flow transects 2 and 3 are marked. (B) Colour denotes interpreted facies. (C) Basal grain size at each core site. (D) Sea floor topography (grey shaded area) overlain with sea floor gradient (red line) along the axis of the Agadir Basin.
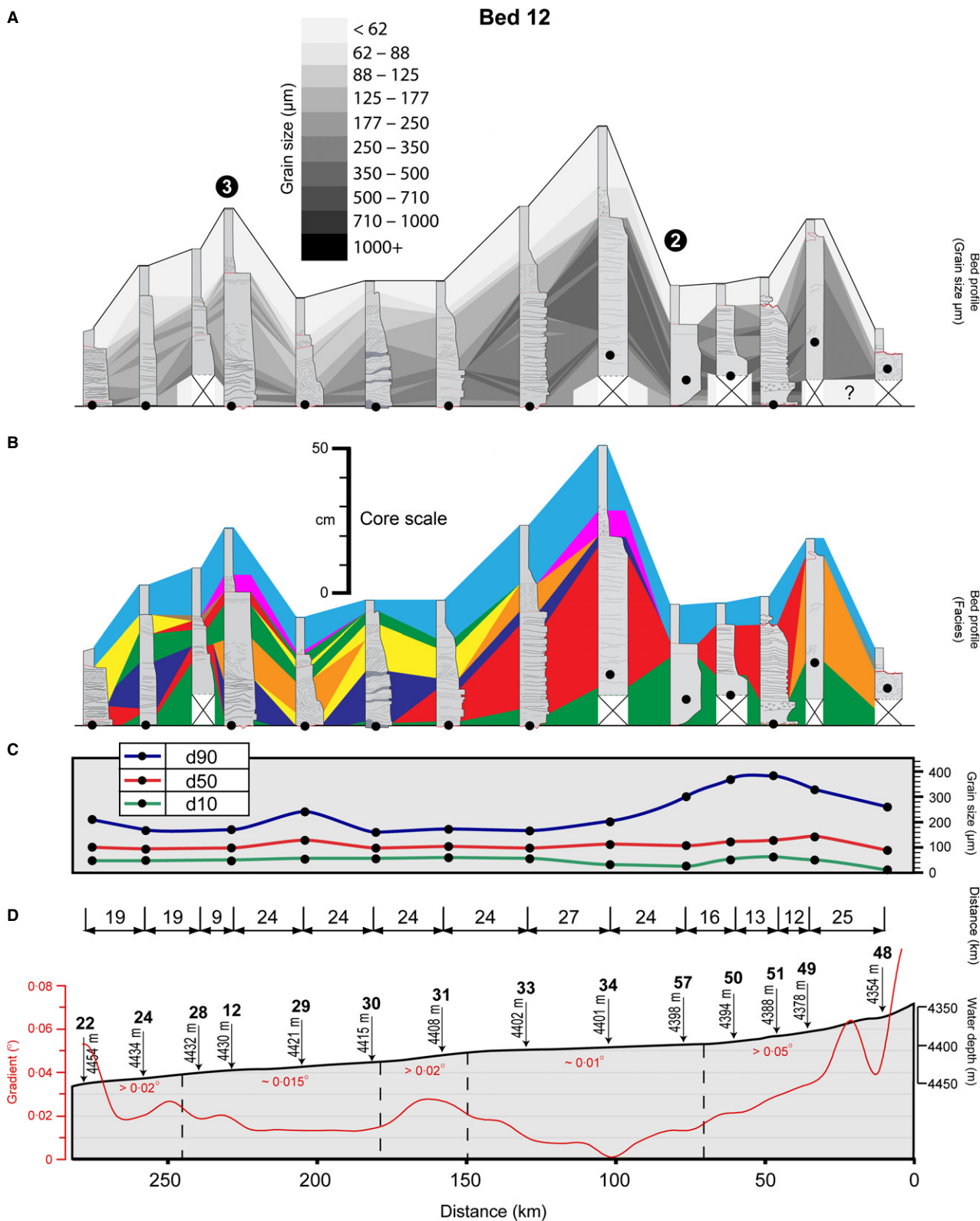
Fig. 12. Bed A12 transects 2 (Proximal) and 3 (Distal) from NW to SE across the Agadir Basin. Graphic logs are anchored onto a horizontal surface to highlight changes in bed thickness. White-crossed areas indicate poor core recovery. (A) and (D) Vertical and spatial distribution of grain size. Position of transect 1 is marked. (B) and (E) Colour denotes interpreted facies. (C) and (F) Sea floor topography (grey shaded area) overlain by sea floor gradient (red line). Vertical exaggeration *ca* 160 times.
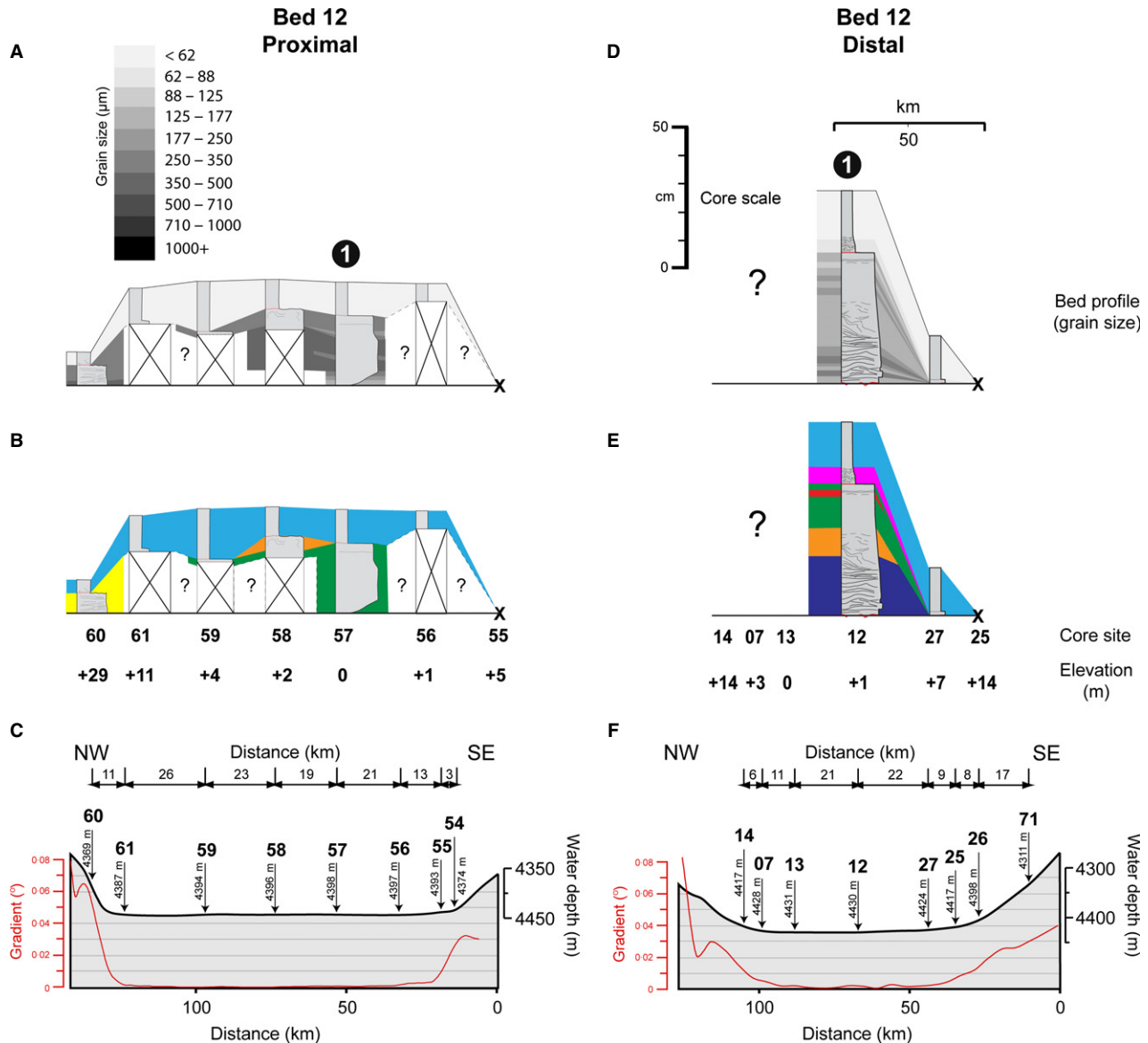
broaden the 5 μm mode or increase the modal grain size to higher values. Traces of coarser grained sediment (*ca* 35 to 70 μm) from flows will generate anomalously high frequencies within what would otherwise be the lowest frequency grain-size range. None of the core sites (25, 26, 54 and 55) contained grain-size distributions, indicating small amounts of sediment being deposited from submarine flows in these locations.

DISCUSSION

Estimating flow thicknesses: What do lateral pinch outs represent?

Having established the lateral extent of flow deposition along the basin margins, it is now important to understand the processes governing how far deposits can drape up topography. Close to the mouth of the Agadir Canyon, Beds

Table 2. Summary of various measured and interpreted aspects of Beds A3 to A12. Note that estimates for total bed volumes include the Agadir Basin (AB) and Madeira Abyssal Plain (MAP). Bed volumes and sand to mud ratios are estimated from the total volumes for sand and mud found across the Agadir Basin and Madeira Abyssal Plain (this study; Frenz *et al.*, 2008; Wynn *et al.,* 2010). Height to which deposits drape up the basin margins, maximum grain sizes found in each bed, and bed geometries are taken from Figs 4, 6, 8, 10 and 12. Interpretations of the character of the flows are based on distribution of facies and bed geometries (discussed further in main text). Note that all beds, except Bed A5, are interpreted to evolve from high concentration to dilute flows with distance downslope.

Bed	Volume AB/MAP/ Total (km³)	Total sand/mud	Sediment	Proximal NW	SE	Distal NW	SE	Maximum grain size (D_{90})	Bed geometry downslope	Proximal	Distal
				Maximum height to which deposits drape up basin margins (m)						Interpreted flow concentration	
3	5/0/5	10/90	Sand Mud	11 to 29 >29	0 to 1 <24	N/A <3	33 to 120 33 to 120	470 µm	Tabular then abruptly thinning	High	Low
5	22/30/52	40/60	Sand Mud	>29 >29	5 to 24 5 to 24	>14 >14	14 to 33 14 to 33	960 µm	Clean sands – tabular Mud-rich sands – lenticular	High	High
7	10/110/120	10/90	Sand Mud	11 to 29 >29	>24 >24	0 to 3 >3	14 to 33 >120	150 µm	Progressive thinning to tabular	High	Low
11	8/0/8	25/75	Sand Mud	>29 >29	0 to 1 1 to 5	N/A ?	N/A 1 to 7	640 µm	Abruptly thinning to tabular	High	Low
12	9/190/200	15/85	Sand Mud	>29 >29	0 to 5 1 to 5	? ?	1 to 7 7 to 14	391 µm	Progressive thinning to tabular	High	Low

A5, A11 and A12 drape higher up the north-west basin margin than along the south-east basin margin. The entry point of turbidity currents was oblique to the basin axis (Fig. 1A). Therefore, close to the mouth of the Agadir Canyon, the flows are likely to have run up the north-west basin margin due to their momentum, increasing the height that deposits drape up the slope (Kneller & McCaffrey, 1999). In contrast, the south-east basin margin has not blocked the flows and onlap heights along this margin are more likely to record the true thickness of the flows.

The height to which deposits drape along the south-east basin margin can be interpreted in two ways. Firstly, the height to which deposits drape represents the total flow thickness (Fig. 14A). Flow thickness will vary through time as the flow passes, so that the height of the drape records the maximum flow thickness (Fig. 14A; Times 1 to 4). Secondly, flows are considered to be stratified into a lower depositional layer overlain by a non-depositional (bypassing) upper layer (Fig. 14B). This upper layer is likely to be dilute and finer grained compared with the lower layer (Kneller *et al.*, 1999; Kneller & Buckee, 2000; Peakall *et al.*, 2001; Duitt *et al.*, 2002;

Gladstone & Sparks, 2002). In this latter scenario, the height to which deposits drape represents the thickness of the depositional parts of the flows. Initially, the upper parts of the flow are capable of bypassing, so that the drape represents only the lower depositional layer (Fig. 14B; Times 1 and 2). Over time, the flows wane sufficiently to allow the upper layer to become depositional, such that the drape represents only the tail end of the upper parts of the flows (Fig. 14B; Times 3 to 5).

It is difficult to distinguish unequivocally which of these interpretations is correct. Both models could have bypassed sediment through the Agadir Basin, explaining the large volumes of fine-grained material found *ca* 700 km downslope within the Madeira Abyssal Plain (McCave & Jones, 1988; Jones *et al.*, 1992; Rothwell *et al.*, 1992; Weaver *et al.*, 1992; Wynn *et al.*, 2002b; Stevenson *et al.*, 2013, 2014). However, the upper part of the flow might be expected to be slower moving, particularly after travelling hundreds of kilometres across the Agadir Basin, and therefore likely to have deposited some silty or muddy deposits higher up the basin margin. Because no such fine-grained traces are found extending up the basin margin, the present

Table 3. Heights to which individual facies drape up the SE basin margin. See Table 1 for facies codes in the 'Interval Type' column.

Proximal Transect

Interval type	Flow type	Bed 3	Bed 5	Bed 7	Bed 11	Bed 12
ST (muddy)	Debris flow	None	5 to 24 m	None	None	None
ST (clean)	High density	None	5 to 24 m	None	None	<5 m
PL, LXL	Either high or low density	<14 m	2 to 29 m	None	<1 m	None
RXL	Low density	None	None	<2 m	11 to 29 m	>29 m
CL, L, CM, M	Muddy	<120 m	>29 m	>29 m	>29 m	>29 m

Distal Transect

Interval type	Flow type	Bed 3	Bed 5	Bed 7	Bed 12
ST (muddy)	Debris flow	None	7 to 14 m	None	None
ST (clean)	High density	None	25 to 33 m	None	1 to 7 m
PL, LXL	Either high or low density	<14 m	25 to 33 m	None	1 to 7 m
RXL	Low density	None	None	7 to 14 m	None
CL, L, CM, M	Muddy	<120 m	25 to 33 m	>120 m	7 to 14 m

None, facies not present.

authors interpret that the height to which sand and mud deposits drape represents the maximum thickness of the sand-laden and mud-laden parts of the flows.

Qualitative analysis of flow evolution across the Agadir Basin

The external shape and distributions of facies are now used to interpret qualitatively the evolving character of parent flows for the five beds.

Bed A3

The flow that deposited Bed A3 was relatively small-volume (*ca* 5 km^3) with different thicknesses for the sandy basal flow (<2 m) and the upper muddy part of the flow (>24 m; Tables 2 and 3). The presence of thin (6 cm) parallel-laminated sands overlain by, and occasionally interbedded with, structureless sands indicates that the basal part of the flow was most probably of high concentration with relatively high aggradation rates, which were periodically high enough to completely suppress bedform development (Sumner *et al.*, 2008). These sands pinch out abruptly downslope, perhaps because the flow was high concentration (Talling *et al.*, 2012, and references therein), but also because the flow was relatively small in volume (Wynn *et al.*, 2002b). Progressive thinning and fining of muds in a downslope direction suggest that the mud-laden part of the flow was dilute and turbulent (Kneller & Buckee, 2000, and references therein).

Bed A5

The flow that deposited Bed A5 had a large total sediment volume (*ca* 52 km^3; Table 2). It was relatively thin with both the sand and mud parts of the flows being <33 m thick along the south-east basin margin (Tables 2 and 3). The presence of structureless sands often interbedded with parallel-laminated sands indicates that parts of the parent flow were most probably high concentration (Talling *et al.*, 2007b, 2012). The tabular and basin-wide extent of this facies suggests that the flow maintained a relatively high-concentration state for most of the length of the Agadir Basin (Fig. 5B). A lack of fining in basal sands downslope (Fig. 6C) suggests that the flow did not lose much energy as it passed across the basin. The presence of relatively thick (40 to 180 cm) mud-rich structureless sands overlying the cleaner sand facies is interpreted to have been deposited from a genetically linked cohesive debris flow (Talling *et al.*, 2007b). Towards the rear of the flow increasing proportions of cohesive mud within the suspension suppressed fluid turbulence, forming a cohesive plug. Continued flow deceleration increased the thickness of the plug until it was able to freeze 'en masse', producing mud-rich structureless sand (i.e. a linked-debrite) across flatter parts of the basin floor (Talling *et al.*,
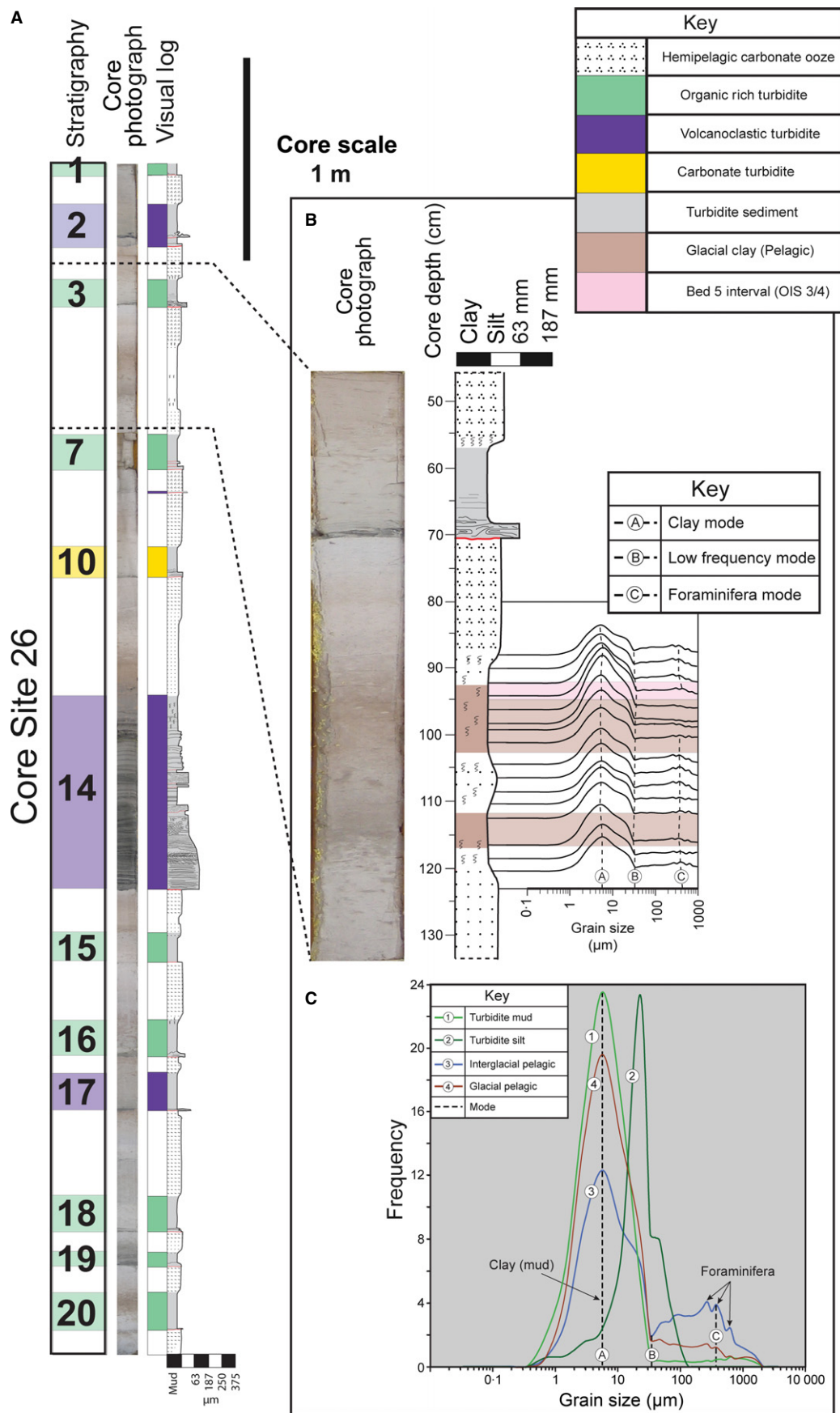
Fig. 13. (A) Examination of basin margin core site 26, illustrating turbidite stratigraphy down core. (B) Grain-size analysis every 1 cm through the interval where Bed 5 should appear (see supplementary material S4). Position where Bed A5 appears in other core sites is shaded pink. Grain size does not change through the interval, indicating no turbidite deposition. (C) Grain-size distributions sampled from nearby Core 12. Bed A5 turbidite mud (1) and silt (2) are shown against interglacial (3) and glacial (4) hemipelagic sediments. Note the low frequency mode in the hemipelagic sediments of *ca* 35 μm, similar grain-size distributions as seen through Core 26 in section (B) of the this figure.

2007b; Wynn *et al.*, 2010; Sumner *et al.*, 2012; Talling, 2013).

Bed A7

The flow that deposited Bed 7 had a large sediment volume (*ca* 120 km^3). The sandy and muddy parts of the flow were >24 m thick (Tables 2 and 3). Close to the mouth of the Agadir Canyon, thin (6 to 15 cm) parallel-laminated sands occur, inter-bedded with intervals of structureless sand. This indicates that the parent flow was most probably high concentration and moving fast enough to develop plane beds with aggradation rates periodically high enough to suppress bedform development (Sumner *et al.*, 2008). The parallel-laminated and structureless sands have a localized thickness maximum at Core 50 (Fig. 7). Downslope, these facies quickly thin and grade into ripple cross-laminated sands, which maintain both thickness and grain size across the rest of the basin (Fig. 7). The association of parallel-laminated and structureless sands with a localized thickness maximum (Fig. 7B) and coarse-tail grading downslope (7C) supports the interpretation that the parent flow was high concentration (Talling *et al.*, 2012, and references therein). Downslope grading into ripple cross-laminated sands indicates that the flow became dilute along its pathway. The ripple cross-laminated sands are uniform in thickness and grain size (Fig. 7B and C) indicating that, once dilute, the flow maintained a relatively constant speed across the rest of the basin. Towards its tail, the flow waned sufficiently to deposit its fine-grained sediment load. It deposited inter-laminated silts and muds first, then with an increasingly clay-rich suspension, ungraded structureless mud (Piper, 1972, 1978; Stow & Shanmugam, 1980; Stow & Piper, 1984; McCave & Jones, 1988; Jones *et al.*, 1992). Contorted mud facies found in Bed A7 are asymmetrically developed with thickness maxima towards the basin margins (Fig. 8B and E). This suggests that the contorted mud caps were most probably first deposited on the basin margins as inter-laminated silts and muds, but became unstable and were remobilized as fine-grained debris flows to flatter areas of the basin.

Bed A11

The flow that deposited Bed 11 was small-volume (*ca* 8 km^3) and relatively thin. The basal, sand-laden part of the flow was <1 m thick, whilst the upper mud-laden part was 1 to 5 m thick (Tables 2 and 3). Inter-bedded structureless and parallel-laminated sands found close to the mouth of the Agadir Canyon indicate that the basal (sand-laden) parts of the flow were most probably high concentration with aggradation rates sufficiently high to periodically suppress bedform development (Sumner *et al.*, 2008, 2012). These structureless and parallel-laminated sands abruptly thin, which is a common geometry observed in sands interpreted to have been deposited from high-concentration flows (Sumner *et al.*, 2012; Talling *et al.*, 2012). Downslope, the thin sands are still parallel-laminated but show a progressive thinning and coarse-tail grading, and then grade into ripple cross-laminated sands (Fig. 9B and C). This change in bed geometry and ultimately sedimentary facies indicates that the parent flow was most probably dissipating; progressively depositing its sediment load until it becomes dilute enough to develop ripple bedforms (Allen, 1982). The mud cap overlying the sands was most probably deposited by the thicker upper part of the flow, which was dilute and turbulent (Kneller & Buckee, 2000). This dilute upper layer was able to bypass proximal parts of the basin, and deposited progressively thicker muds downslope (Fig. 9).

Bed A12

The flow that deposited Bed 12 had a large sediment volume (*ca* 200 km^3) that was mostly fine-grained mud and silt (*ca* 190 km^3; (Frenz *et al.*, 2008). It had different thicknesses for its lower sandy parts (<5 m) and its upper muddy parts (7 to 14 m; Table 2). In proximal parts of the basin, deposits of structureless and parallel-laminated sands suggest that the basal parts of the parent flow were most probably high concentration with aggradation rates sufficient

Flow is depositional throughout its vertical structure
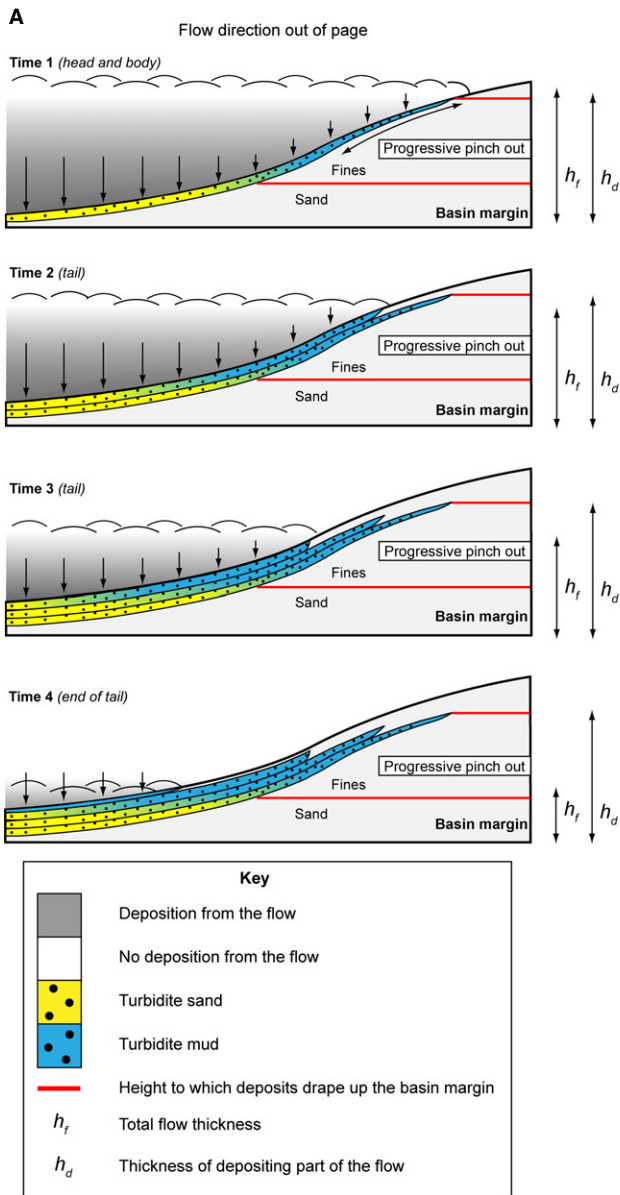
2-layer flow with depositional lower part and non-depositional (bypassing) upper part
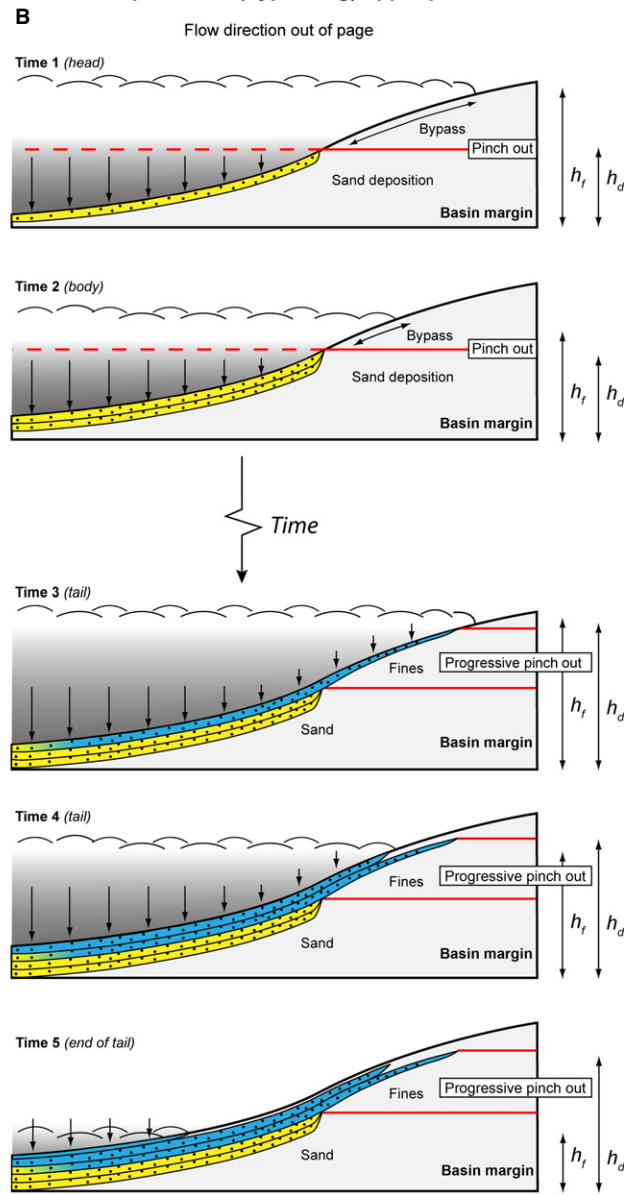
Fig. 14. An across-flow schematic illustrating two models that interpret the height to which sand and mud deposits drape up the basin margin. (A) Flow is depositional throughout its vertical structure with sand and mud progressively pinching out up the basin margin. The different heights to which sand and mud drapes represents the different heights they were suspended above the bed within the flow. As flow thickness will change over time (Time 1 to Time 4), the height to which deposits drape represents the maximum thickness of the flow during its passage. (B) Two-layer flow with a lower depositional layer, which is sand-laden, overlain by a non-depositional (bypassing) upper layer, which is laden with fine-grained sediment (Time 1 and Time 2). In this case, the height to which deposits drape represents the lower depositional parts of the flow, not the total flow thickness. With time the flow wanes, enabling the upper layer to become depositional (Time 3 to Time 5). Hence, the height to which fine-grained deposits drape the basin margin represents the thickness of the tail of the flow.

to suppress bedform development. The basal grain sizes of these sand facies exhibit coarse-tail grading to *ca* 100 km downslope (Fig. 11C), suggesting that the flow was losing energy. After the 100 km mark, basal sands maintain a relatively constant grain size with a concomitant grading of facies into low-angle and ripple cross-laminated sands. This indicates that the

parent flow was probably evolving into a more dilute suspension with distance downslope (Allen, 1982). Although the flow was becoming dilute, its speed remained fairly constant, producing deposits with relatively uniform basal grain sizes across the rest of the basin. Structureless sands with thin mud-rich bands are found overlying ripple cross-laminated sands in the distal parts of the basin (for example, Core 12; Fig. 11B). This may have been the result of sediment slowly concentrating near to the bed towards the rear of the flow. With sufficient concentrations of sediment, turbulence would be damped and the suspension would rapidly 'collapse' onto the bed, producing a structureless deposit. Towards the tail, the flow waned sufficiently to allow deposition of fine-grained sediment. It first deposited inter-laminated silts and muds, then with an increasingly clay-rich suspension, ungraded structureless mud (Piper, 1972, 1978; Stow & Shanmugam, 1980; Stow & Piper, 1984; McCave & Jones, 1988; Jones *et al.*, 1992). However, the flow efficiently bypassed most of its fine-grained sediment *ca* 700 km downslope into the Madeira Abyssal Plain (Wynn *et al.*, 2002b; Stevenson *et al.*, 2013), resulting in a relatively thin mud cap across the Agadir Basin (Fig. 11B).

Comparison to previous estimates of flow thickness

Flow thicknesses have been documented by previous work using flow deposits or erosional trim lines, and direct monitoring of active flows (Talling *et al.*, 2014, tables 1 and 2). Flow thickness can be highly variable, and strongly depends on the degree of lateral confinement in channels or canyons, and the total volume of sediment within the flow. Other factors such as sea floor gradient, flow speed and concentration, grain sizes present, and hence rates of mixing with sea water, can also significantly affect flow thickness.

The only information on flow thickness for events such as these in the Moroccan Turbidite System, triggered by large landslides, comes from the Grand Banks event in 1929. Erosional trim lines recorded a thickness of 160 to 270 m in fan-valleys (Hughes Clarke, 1988). However, the thickness of this flow as it spread across the distal abyssal plain is unknown. Flows that are strongly confined within submarine canyon and channel systems can be many tens to several hundred metres thick, such as in Monterey Can-

yon (50 to 80 m thick; Xu *et al.*, 2004), Hueneme and Mugu Canyons (15 to 25 m; Xu *et al.*, 2010), Gaoping Canyon (150 m thick; Liu *et al.*, 2012), Zaire Canyon-channel (120 to 140 m; Khripounoff *et al.*, 2003; Vangriesheim *et al.*, 2009), 1979 in Var Canyon (30 to 50 m in the upper canyon and 120 m in the lower canyon; Khripounoff *et al.*, 2009), Northwest Atlantic Mid-Ocean Channel (120 to 280 m thick; Klaucke *et al.*, 1997) and the Amazon Channel (30 to 280 m thick; Hiscott *et al.*, 1997; Pirmez & Imran, 2003). The more powerful (canyon and channel) confined flows can sometimes travel at speeds of 2 to 20 m sec^{-1} and reach speeds of *ca* 1 m sec^{-1} at heights of 50 to 150 m above the bed, with sand transported 40 to 50 m above the bed (Khripounoff *et al.*, 2003; Vangriesheim *et al.*, 2009; Liu *et al.*, 2012). In other locations, core transects suggest that sand deposition is restricted to <5 to 10 m above the bed in canyon heads (Paull *et al.*, 2005). Bowen *et al.* (1984) mapped the height to which two turbidite beds draped up channel margin topography within the Navy Fan, offshore California. These authors concluded that the mud-rich bed (*ca* 3% sand) was deposited by a flow 15 to 75 m thick, whilst the bed with a higher sand component (*ca* 42% sand) was deposited by a flow <10 m thick. Flows confined within delta front channels can be up to a couple of tens of metres thick, such as in Bute Inlet (7 to 14 m; Prior *et al.*, 1987) and on the Squamish River Delta (10 to 40 m; Hughes Clarke *et al.*, 2012; Clarke, 2014). Turbidity currents that have been monitored in lakes and reservoirs tend to be rather slow (<50 cm sec^{-1}), dilute (<0·01% volume) and have thicknesses of less than 16 m (Talling *et al.*, 2014).

The flows that contained the highest percentage of mud (Beds A3 and A7) may have been locally 120 m thick, and were consistently thicker than *ca* 30 m. Both the mud and sand carrying components of Bed A5 were between 5 m and 33 m thick. However, the Bed A11 and A12 flows were relatively thin. Bed A11 only reached heights of 5 to 7 m, whilst Bed A12 drapes to heights of less than 5 to 14 m up the basin margin, despite transporting an extremely large volume (*ca* 200 km^3) of sediment. All of these beds extend across the full width (100 to 150 km) of the Agadir Basin. This may explain why some flows were so thin, despite carrying very large sediment volumes, and why their thickness is similar or smaller than that of less voluminous flows in confined channel or canyon settings.

What controls flow thickness in the Agadir Basin?

Previous studies have suggested that flow thickness is a function of grain size and flow volume, with finer-grained or larger-volume flows tending to be thicker (e.g. Bowen *et al.*, 1984; Normark *et al.*, 2009). However, the present study did not find a simple correlation between either grain size or flow volume and flow thickness (Fig. 15).

Beds A3 and A7 contain the lowest proportion of sand (*ca* 10%) and were deposited by relatively thick flows (consistently thicker than 30 m). In contrast, Beds A11 and A12 contain a higher proportion of sand (10 to 25%) and were deposited by thinner flows that did not extend more than 14 m up the basin margins. However, Bed A5 contains the highest proportion of sand (*ca* 40%) and drapes 24 to 33 m up the basin margins, further than Beds A11 and A12. If the proportion of sand within a flow alone controls flow thickness, then Bed A5 would be expected to be the thinnest flow.

The smallest volume bed (Bed A3; 5 km³) reaches heights of more than 30 m up the basin margin. However, Bed A11 has a similar volume (8 km³), but only extends to heights of <7 m up the basin margin (Fig. 15B). Bed A5 (52 km³) and
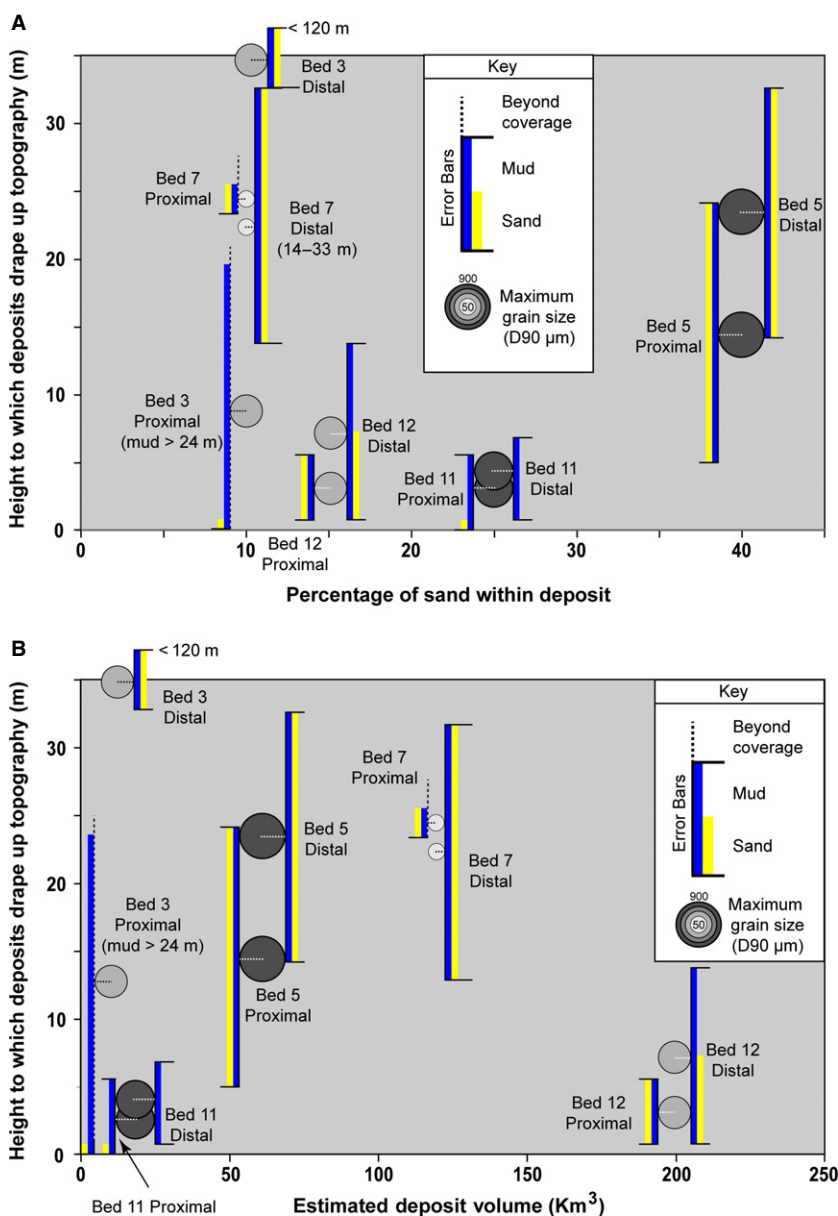
Fig. 15. Graphs showing the height to which deposits drape up the south-east basin margin, interpreted to be a measure of flow thickness. Error bars (blue and yellow) show where deposits pinch out up topography, and are constrained by elevations between core sites. Mid-points within the error bars show maximum grain size measured in the bed (Table 2). White dashed lines connect error bars with the associated grain-size measurement for each bed. Height to which deposits drape up basin margin topography is plotted against: (A) total sand fraction within the bed (measured from the total estimated deposit volume); and (B) total estimated deposit volume, including bed volumes from the Agadir Basin and Madeira Abyssal Plain (after Wynn *et al.*, 2002b; Frenz *et al.*, 2008; Wynn *et al.*, 2010). Note the poor correlation in both cases.

Bed A7 (120 km³) have much larger volumes. Both sand and mud in Bed A5 reach heights of 24 to 33 m. The sand in Bed A7 also reaches elevations of *ca* 30 m, although its mud can extend to heights in excess of 120 m. However, the largest volume bed (Bed A12; 200 km³) only drapes to heights of <14 m up the basin margins. In proximal locations, the Bed 12 event was less than 5 m thick. If volume alone governed flow thickness, then it would be expected that Bed A12 would be the thickest flow. The lack of a simple correlation between grain size or flow volume and overall flow thickness suggests that other, perhaps interdependent, factors are important in determining flow thicknesses. For example, sea floor gradient, flow speed and sediment concentration can influence rates of mixing with sea water, which can significantly affect flow thickness. However, the present authors note that the height to which deposits pinch out is similar in the proximal and distal transects (*ca* 100 km apart) for individual beds (Table 2), indicating that flows maintained their thickness across the basin. A lack of downslope thickening of the flows suggests that rates of mixing with sea water were low.

Quantitative constraints on bed shear velocity and flow speeds

This section quantitatively estimates the shear velocity beneath the flows that deposited Beds A3, A5, A7, A11 and A12. Two independent approaches are employed. Firstly, shear velocity is calculated from inferred flow thicknesses and slope for a range of flow densities, assuming that momentum is not inherited from further upslope and that viscous forces can be neglected. Secondly, shear velocities are calculated from the grain sizes measured in the basal sands of the flow deposits.

Downslope component of the gravitational force driving the flow

It is possible to approximate near-bed shear stress (τ_o) beneath submarine flows from the component of the downslope directed gravitational driving force of the flow (the excess weight of the flow) that is parallel to the bed via:

$$\tau_o = (P_f - P_a)g'H_f \sin\theta \qquad (1)$$

where τ_o is the shear stress at the base of the flow, $\sin\theta$ is the downslope sea floor gradient, reduced gravity (g') is given by the bulk density

difference between the flow density (P_f) and the density of ambient sea water (P_a) multiplied by gravitational acceleration (g) and H_f is the thickness of the flow (inferred from the lateral pinch outs of deposits). In this approach, it is appropriate to use the full thickness of the flow (Abad *et al.*, 2011; Darby & Peakall, 2012; Dorrell *et al.*, 2013). This analysis assumes a uniform flow and ignores the upper interface between the flow and ambient fluid. The bed shear velocity (U^*_f) is related to the bed shear stress (τ_o) via (Bagnold, 1966; Komar, 1985; Garcia & Parker, 1993; Leeder, 1999):

$$U^*_f = \sqrt{\frac{\tau_o}{P_f}} \qquad (2)$$

This leads to the following equation (Kneller, 2003; Eggenhuisen & McCaffrey, 2012):

$$U^*_f = \sqrt{H_f g \left(\frac{p_f - p_a}{p_a}\right) \sin\theta} \qquad (3)$$

The assumptions behind this equation deserve careful consideration. Firstly, this approach assumes that the flow is uniform and ignores frictional retardation, such as due to mixing at the upper interface between the flow and ambient fluid. Frictional retardation is included in a later relation (Eq. 4) between bed shear velocity and mean flow velocity (U) via the drag coefficient (C_D). Secondly, Eq. 3 does not account for the dissipation of momentum acquired further upslope. For instance, it predicts that flows will not pass across horizontal gradients, nor be able to travel upslope. There is field evidence that flows can sometimes travel for long distances (>100 km) upslope, including in the Agadir Basin, due to inherited momentum (Underwood, 1991; Talling *et al.*, 2007a; Hunt *et al.*, 2011). Thirdly, the effects of flow viscosity and yield strength are neglected. This may be a reasonable assumption for dilute and faster moving flows, but bed shear stresses will start to decrease as sediment concentrations increase above *ca* 9%, especially in flows such as these that contain large volumes of cohesive mud (Talling *et al.*, 2012). In particular, evidence of cohesive debris flow deposition suggests that this equation may not be entirely appropriate for Bed A5 (Talling *et al.*, 2007b).

Since P_a and g are essentially constant, the main factors controlling near-bed shear velocity in Eq. 3 are flow thickness (H_f), bulk density of the flow (P_f) and the slope ($\sin\theta$). Slope is known from GEBCO bathymetry across the basin
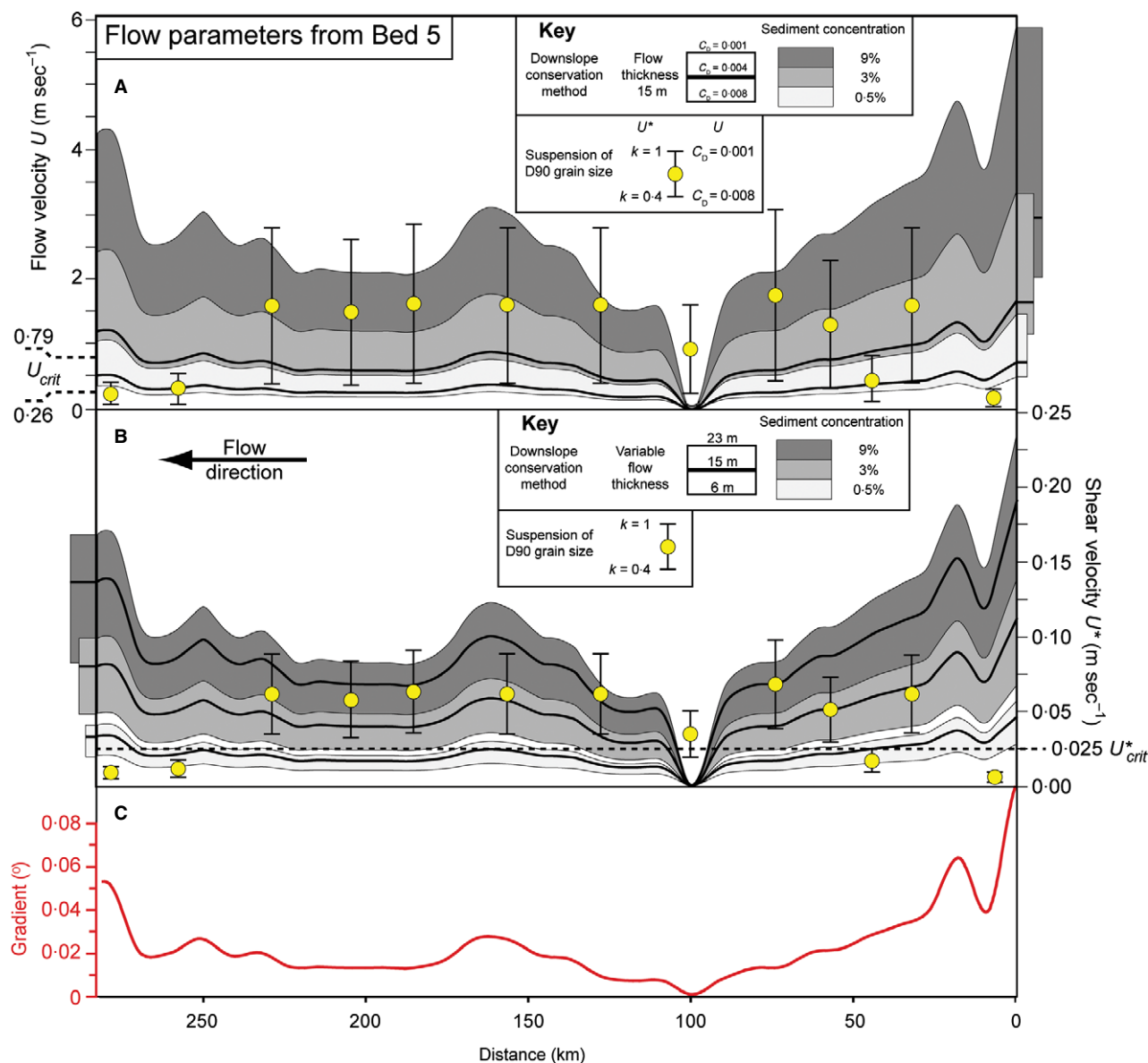
Fig. 16. Modelled flow parameters derived from Beds A5 and A12. The white bottom parts (C) and (F) show slope running down the axis of the Agadir Basin. Parts (B) and (E) show reconstructed flow shear velocities ($U*_f$) calculated from: (i) downslope gravitational driving force, where grey shading represents different bulk flow densities and the bounds of shading show the effects of variations in flow thickness; and (ii) grain-size suspension criteria, where coloured circles represent the middle calculated values and error bars show the range of uncertainty in the calculation (see main text for details). Parts (A) and (D) use modelled flow shear velocities from (B) and (E) to reconstruct actual flow speeds (U_f). Uncertainty is increased due to the range of potential values for the friction coefficient at the base of the flow (C_D). The erosion threshold of exposed hemipelagic sea floor sediments is marked as a critical shear velocity ($U*_{crit}$) on (B) and (E), and as a flow speed (U_{crit}) on (A) and (D).

(Fig. 1C). Flow thicknesses can be constrained for Beds A5, A11 and A12 from the height to which their deposits pinch out up the basin margins. Although, Beds A3 and A7 have deposits that extend beyond the coverage of the cores and so it is not possible to approximate their near-bed shear velocities using this approach. The remaining important control is bulk flow density, which is unknown. Therefore, a range of bulk flow densities are assumed corresponding to layer-averaged sediment volume concentrations of 0·5% (P_f = 1035 kg m^{-3}), 3% (P_f = 1075 kg m^{-3}) and 9% (P_f = 1175 kg m^{-3}). Sediment concentrations are likely to be higher close to the bed, than
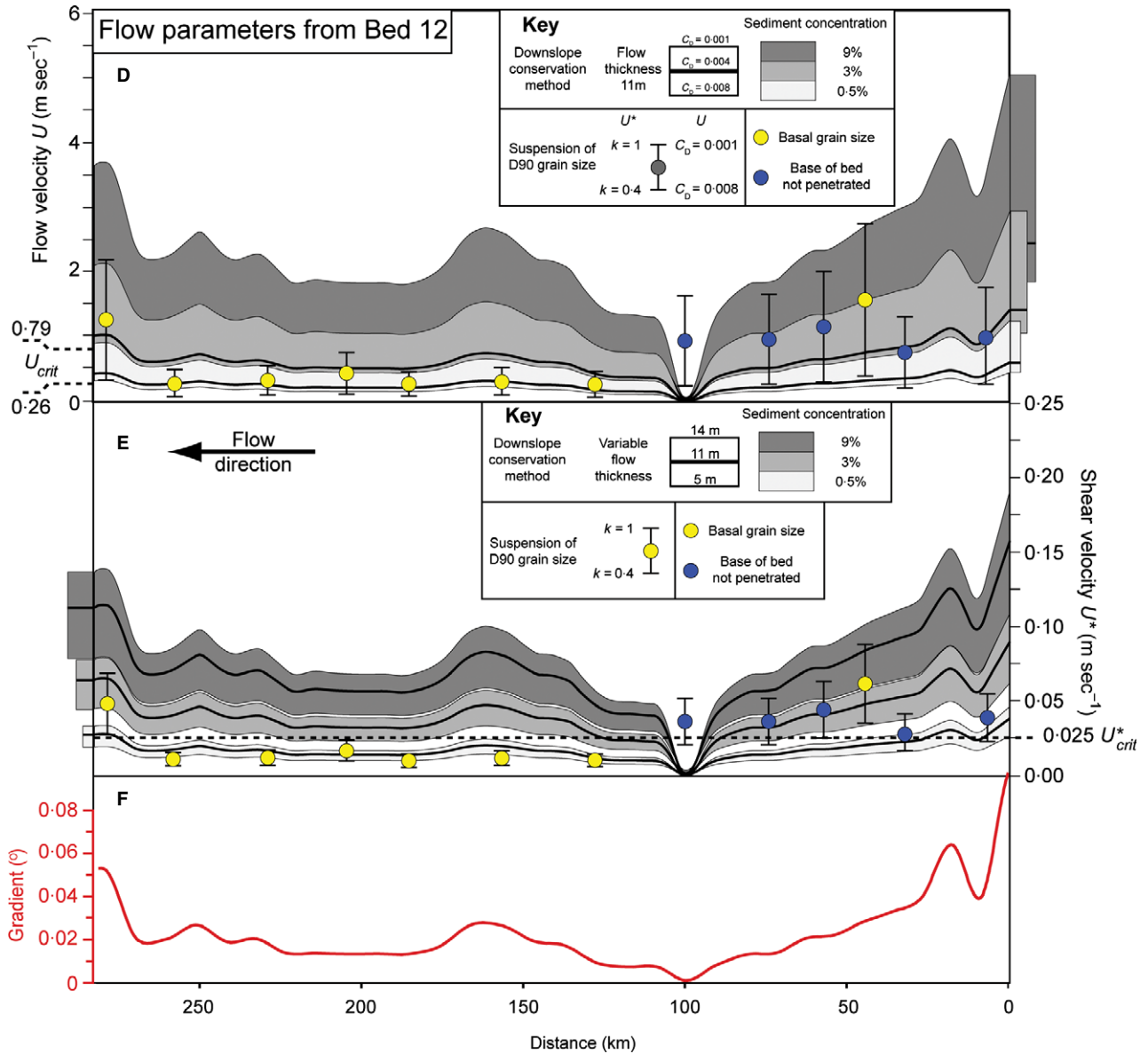
Fig. 16. (Continued)

these layer-averaged concentration values. Grain interactions may mean that the assumptions behind this approach are flawed at concentrations in excess of *ca* 9% volume. These calculations assume a sediment density of 2600 kg m^{-3} and a sea water density of 1027 kg m^{-3}.

Using a range of flow thicknesses and bulk densities allows the uncertainty of these shear velocity estimates to be explored (Fig. 16). In the proximal (steeper) areas of the basin, for the higher layer-average volume concentration (3 to 9%) flow condition, U^*_f values are between 0·05 m sec^{-1} and 0·27 m sec^{-1} from Bed A5, and 0·04 to 0·17 m sec^{-1} from Bed A12, which decrease in both beds

to values of *ca* 0·025 to 0·08 m sec^{-1} in distal (flatter) areas of the basin (Fig. 16B and E). For the dilute (0·05% volume) concentration condition, U^*_f values in both beds are *ca* 0·04 m sec^{-1} in proximal areas, whilst distal areas yield shear velocities of between 0·01 m sec^{-1} and 0·025 m sec^{-1}. In turn, the shear velocity (U^*_f) can be related to forward flow velocity via:

$$U = \frac{U^*_f}{\sqrt{C_D + E_w}} \qquad (4)$$

where U is the downslope velocity of the flow, C_D is the dimensionless friction coefficient at

the bed and E_w is the friction across the upper surface of the flow due to entrainment given by $E_w = 0.072 \sin \theta$ (Pirmez & Imran, 2003). On the shallow slopes (*ca* 0.01 to 0.02°) of the Agadir Basin values of E_w range from 8×10^{-6} to 2×10^{-4}. The value of C_D is difficult to determine because important flow parameters, such as the vertical sediment concentration profile, are not known (Soulsby, 1997). Therefore, a range of values for C_D are considered from 0.001 to 0.008; including those that have been calculated from experiments (Parker *et al.*, 1987; Garcia & Parker, 1993; Thompson *et al.*, 2006; Straub & Mohrig, 2008) and values that have previously been employed to represent the friction coefficient at the base of natural submarine flows (Komar, 1969, 1971, 1973; van Tassell, 1981; Bowen *et al.*, 1984; Komar, 1985; Reynolds, 1987; Pirmez & Imran, 2003; Migeon *et al.*, 2012).

Taking an average flow thickness of 15 m for Bed A5 and 11 m for Bed A12, Fig. 16A and D illustrate the effect of the C_D variable on flow velocity estimates derived from Beds A5 and A12. A dense (3 to 9% layer-averaged) flow travels at between *ca* 1 m sec^{-1} and 4 m sec^{-1} on the steeper slopes, whilst across the flatter parts of the basin flow velocities are between 0.5 m sec^{-1} and 3 m sec^{-1}. The dilute (0.5% layer-averaged) flow condition results in flow speeds of *ca* 0.4 to 0.5 m sec^{-1} on steep slopes followed by flow speeds of 0.2 m sec^{-1} across the flatter areas of the basin (Fig. 16A and D).

Minimum near-bed shear velocity and flow velocity from grain size

Flow shear velocity can be estimated from deposited grain sizes using the following equation (van Tassell, 1981; Bowen *et al.*, 1984; Komar, 1985; Zeng *et al.*, 1991):

$$U_f^* = kW_s \qquad (5)$$

where k is the flow condition at which particles are considered suspended within the flow. Previous studies have generally used values of $k = 1$ for the threshold at which particles are suspended (Bagnold, 1966; Bowen *et al.*, 1984; Komar, 1985). However, lower values for the suspension threshold for sand-sized grains have been determined experimentally ($k = 0.4$; Nino *et al.*, 2003). Accounting for this range, the present study uses values for k between 0.4 and 1 to represent the suspension criterion of

particles. W_S is the particle settling velocity of the coarsest 10% of particles in the deposited grain-size population (D_{90}). Assuming that grains are settling in isolation from a dilute suspension and do not interact, settling velocity is calculated from Soulsby (1997):

$$W_s = \frac{\eta}{d}\left[(10.36^2 + 1.049D_*^3)^{1/2} - 10.36\right] \qquad (6)$$

where η is the kinematic viscosity of water (1.36×10^{-6} m^2 sec^{-1}), d is the diameter of the settling particle (m) and D_* is the dimensionless grain size, given by:

$$D_* = \left[\frac{g(S-1)}{\eta^2}\right]d \qquad (7)$$

where g is acceleration due to gravity (9.81 m sec^{-2}), S is 2.53, which represents the ratio of densities of particle (assumed to be silica sand 2600 kg m^{-3}) and sea water (1027 kg m^{-3}). These calculations use D_{90} (rather than D_{50} or D_{10}) because it represents the higher shear velocities within the flow (van Tassell, 1981, 1986). Furthermore, using D_{90} has produced flow speed estimates that best match directly measured flow speeds (Zeng *et al.*, 1991).

The values calculated from deposited grain sizes are minimum estimates of bed shear velocity (or flow velocity) for two reasons. Firstly, a value of $k = 0.4$ is for the onset of weak suspension (Nino *et al.*, 2003). It is likely that higher values of k would be needed to suspend sand several metres or tens of metres above the bed. Secondly, larger grains may not have been available for transport within the flow. In this case, the flow would have transported larger grains had they been present. It is also noted that the size of grains suspended may also depend on sediment concentration (flow capacity) as well as flow speed or bed shear velocity (Kuenen & Sengupta, 1970; Hiscott, 1994). The influence of sediment concentration on the size of grains suspended or deposited is neglected here. The base of Bed A12 was not penetrated in some cores (Fig. 16D and E, blue dots). Therefore, the base of the bed may have contained coarser sediment.

Using the D_{90} grain size of basal sands from Bed A12, estimated U_f^* in proximal parts of the basin are *ca* 0.020 to 0.09 m sec^{-1}. This is followed by U_f^* values of *ca* 0.02 m sec^{-1} across more distal parts of the basin (Fig. 16E). Via Eq. 5, these U_f^* values provide estimates of flow

velocity (U) of *ca* 0·25 to 2·80 m sec^{-1} in proximal parts of the basin and *ca* 0·10 to 0·50 m sec^{-1} in distal parts of the basin (Fig. 16D). Bed A5 is exceptionally coarse-grained compared to the other beds in this study. Therefore, shear velocities and downslope flow velocities derived from the deposits of Bed A5 yield significantly higher values compared to Beds A3, A7, A11 and A12 (for example, Bed A12; Fig. 16D and E). In general, Bed A5 provides $U*_f$ values that are between *ca* 0·03 m sec^{-1} and 0·09 m sec^{-1} throughout the basin (Fig. 16B) with corresponding flow speeds of U = 0·5 to 3 m sec^{-1} (Fig. 16A).

In general, minimum values of bed shear velocity from the suspension criteria (Eq. 5) are consistent with bed shear velocities derived from flow thicknesses and gradients (Eq. 3), for flows with a range of layer-averaged sediment concentrations between 0·5% and 9% (Fig. 16). For Bed A5, shear velocity estimates from grain size fall within layer-averaged concentrations of 3 to 9%. Although in proximal core sites 48 and 51 (Fig. 1B; Fig. 5), shear velocity estimates from grain size are low compared to those derived from flow thickness and slope (Fig. 16B). These discrepancies between estimated shear velocities correspond with localized hiatuses beneath Bed A5 (Fig. S1) (Talling *et al.*, 2007b). For Bed A12 in the distal basin (Fig. 16E), minimum bed shear velocities needed for sediment suspension are consistently similar to bed shear velocities estimated from Eq. 3 for dilute (0·5% volume concentration) flows.

Calculating flow speeds required to erode the sea floor

There is no significant (<1 to 2 cm) differential erosion beneath Beds A3, A7, A11 and A12 across the Agadir Basin; although closer to the mouth of the Agadir Canyon, Bed A5 directly overlies a major erosion hiatus (Fig. 1A) (Talling *et al.*, 2007b; Macdonald *et al.*, 2011). Therefore, calculating erosion thresholds for the hemipelagic (sea floor) sediments provides estimates for maximum near-bed shear velocities beneath turbidity currents passing across the basin floor. Crucially, this method assumes that the hemipelagic mud is exposed to the flow, and is not buried beneath initial flow deposits.

Resistance to erosion is measured via the critical bed shear stress ($\tau_{o\text{-crit}}$), above which erosion starts to occur. In mud, this resistance is controlled by the interaction of the physical, geochemical and biological properties of the

sediments (see Grabowski *et al.*, 2011, for a review). In general, there is a positive relation between bulk sediment density and critical shear stress (Mitchener & Torfs, 1996). Bed density is determined by the physical properties of the sediment, such as grain size, shape and packing structure (Miller *et al.*, 1977), and consolidation processes, whose effects are influenced by the sand : mud ratio of the sediment (Ockenden & Delo, 1988), time (Halka *et al.*, 1991) and the cohesive components of the bed. Cohesive components are a complex function of several factors such as clay mineral composition, chemistry of the pore water and structure of the sediment, and duration for consolidation (Parchure & Mehta, 1985; Mitchener & Torfs, 1996; Whitehouse *et al.*, 2000, and references therein; Aberle *et al.*, 2004). Biological activity can stabilize the bed via biofilms and algal mats, and from increased organic content within the sediment, which can dramatically increase the cohesiveness and, in turn, the critical shear stress of the bed (Tolhurst *et al.*, 1999; Aberle *et al.*, 2004; Quaresma *et al.*, 2004). Because of the complex interactions among these influential factors, it is hard to obtain reliable results from laboratory tests, which typically predict higher critical shear stresses than found in natural sediments (Mitchener & Torfs, 1996; Tolhurst *et al.*, 2000). Hence, *in situ* measurements are the most appropriate means to determine critical bed shear stresses in natural sediments. However, values of critical shear stress in natural sediments are wide ranging because of site-specific fluctuations in the factors outlined above. Currently, there are no published *in situ* measurements of critical erosion stresses for deep-water hemipelagic sediments. Limited information is currently available on the Agadir Basin hemipelagic sediments regarding their mineral composition, organic content or biological activity. Only bulk density and grain-size data are available to estimate their critical shear stress. Therefore, the present authors approximate the critical shear stresses of deep-water hemipelagic sediments to those determined from a range of *in situ* measurements in muddy shallow marine environments with similar grain sizes and bulk densities (Brommer *et al.*, 2009; Amos *et al.*, 2010). It is noted herein that the bulk density values for the hemipelagic sediments are taken from gamma-ray measurements from the top 10 cm of the cores in the Agadir Basin (Fig. S5). The piston coring technique used in the Agadir Basin may not recover the uppermost sediments (i.e. within *ca* 10 to

20 cm of the sea floor surface); hence, the bulk densities measured in the cores are likely to be higher than those in the sediments immediately below the sea floor. This likely overestimation of hemipelagic sediment density directly below the sea floor may overestimate the critical shear stress needed for erosion.

Firstly, the bulk density of hemipelagic sediment is related to an erosion threshold via a critical shear stress ($\tau_{\text{o-crit}}$) using an empirical relation from Amos *et al.* (2010, equation 11a):

$$\tau_{\text{o-crit}} = \left[5{\cdot}44 \times 10^{-4} P_{\text{b}}\right] - 0{\cdot}28 \qquad (8)$$

where $\tau_{\text{o-crit}}$ is the critical shear stress and P_{b} is the wet bulk density of the sea floor sediment (kg m^{-3}). Gamma-ray measurements within the uppermost 10 cm of cores from the Agadir Basin show bulk densities of hemipelagic sediments ranging between *ca* 1200 kg m^{-3} and *ca* 1700 kg m^{-3} (Fig. S5). To calculate an upper limit of the sea floor erosion threshold, a value of $P_{\text{b}} = 1700$ kg m^{-3} is used; corresponding to a $\tau_{\text{o-crit}}$ value of 0·64 Pa. Via Eq. 2, this critical shear stress is related to a critical shear velocity (U^*_{crit}), required to erode sea floor sediments. The present authors assume a range of bulk flow densities between 1035 kg m^{-3} and 1175 kg m^{-3} corresponding to sediment concentrations of *ca* 0·5 to 9%, respectively (assuming a sediment density of 2600 kg m^{-3} and sea water density of 1027 kg m^{-3}). This range of flow densities yields sea floor erosion thresholds between $U^*_{\text{crit}} = 0{\cdot}025$ m sec^{-1} and 0·023 m sec^{-1}, respectively (with the upper limit marked on Fig. 16B and E). From Eq. 4, this range of shear velocities represents flow speeds of between 0·79 m sec^{-1} and 0·26 m sec^{-1}, which are marked on Fig. 16A and D.

Comparing estimated flow velocities to sea floor erosion parameters

Now, the critical shear velocity estimated for erosion of sea floor sediments (U^*_{crit}) is compared to shear velocities calculated at the bases of the flows (U^*_{f}). In proximal parts of the basin, estimations of shear velocity, from the downslope gravitational driving force (Eq. 3) and those based on grain-size suspension criteria (Eq. 5), exceed the critical shear velocity required for sea floor erosion (Eqs 6 and 7) (Fig. 16). The exception is in the distal part of Bed A12, where values of bed shear velocity from the sediment suspension criteria (Eq. 5) and from the down-

slope gravitational driving force (Eq. 3) for dilute (0·5% volume concentration) flow are consistent with a lack of erosion ($U^*_{\text{f}} < 0{\cdot}25$ m sec^{-1}).

This raises the question; how did these flows travel across the proximal (and in some cases distal) Agadir Basin without eroding significantly into the sea floor mud? Two explanations are offered here. Firstly, the flows were fast enough to erode into the hemipelagic mud, but sediment previously deposited from the flow shielded the hemipelagic mud from erosion (Fig. 17A). This model implies that the flow was depositional from the moment it arrived at a location. Secondly, it is possible that one or more of the assumptions made in the calculations herein are invalid. For instance, the presence of high-concentration near-bed layers (Fig. 17B) would
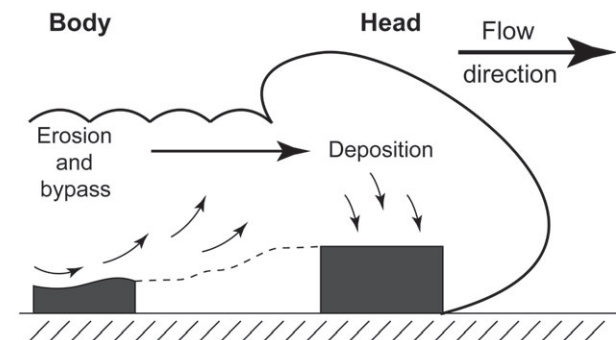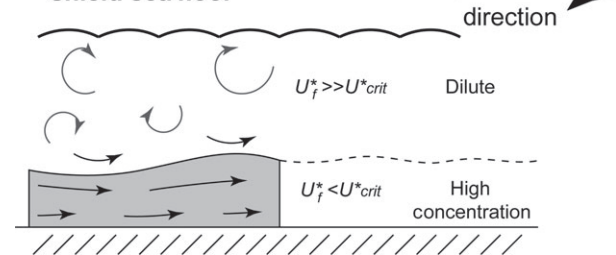
Fig. 17. Conceptual models of the flow processes responsible for armouring the sea floor against erosion. (A) The flow is initially depositional as it arrives at a given location. Deposited sediment armours the sea floor against erosion by the rest of the flow, which is able to erode and bypass sediment downslope. (B) High sediment concentrations near to the bed may suppress turbulence and support grains via other mechanisms, meaning that the flow could suspend its sediment load at lower shear velocities. In addition, high-concentration layers would shield the sea floor from potential erosion from the overriding upper parts of the flow.

suppress turbulence and support grains through hindered settling; meaning that settling velocities (W_s) calculated from Eqs 4 and 5 would be over-estimated and near-bed shear velocities could be significantly lower, allowing flows to travel relatively slowly yet still suspend their sediment loads. In addition, high near-bed sediment concentrations could also significantly reduce friction (C_D) at the bed (Thompson *et al.*, 2006), allowing the flow to travel faster without having sufficient shear velocity (Eq. 2) to erode into sea floor mud.

CONCLUSIONS

This contribution documents the character of five individual submarine flow deposits that extend for over 250 km along the Agadir Basin offshore north-west Africa, and 100 km across its width. It uses the heights to which deposits drape up basin margins to place constraints on flow thicknesses. This is the only field data set where the external bed shape, internal distribution of lithofacies, changes in grain sizes and sea floor gradient, bed volumes, flow thickness and depth of erosion into underlying hemipelagic mud are known for individual submarine flow deposits. Because it will be difficult to collect a more complete data set for individual flow deposits, this is an important data set for understanding how these flows evolved and for comparison to numerical or physical models.

Deposit volume, maximum grain size within the bed, and sand : mud ratio within individual beds did not correlate strongly with inferred flow thicknesses. The two flow deposits (Beds A3 and A7) with the largest proportions of mud were most probably over 30 m thick, and locally up to 120 m thick. Bed A5 comprises both turbidity current and cohesive debris flow deposits, and sand and mud layers within this bed drape to heights of up to 30 m up the basin margins. The two flows with the highest fraction of sand (Beds A11 and A12) were much thinner, with flow thicknesses of less than 5 to 14 m. Sand was most likely to be carried in the lower 5 to 7 m of these flows. It is surprising that the Bed A12 event was so thin given that it transported a very large volume of sediment (>200 km^3) for long distances across a very flat basin floor.

Field observations show that these (sometimes thin) flows suspended sand several metres to tens of metres above the sea floor, and efficiently transported it for up to 250 km along the basin

axis. Near uniform hemipelagic mud interval thickness between beds, and uniform coccolith assemblages in the mud caps of the beds, suggest that the flows did not erode significantly into the underlying sea floor mud across the basin plain.

Simple calculations were made of near-bed shear velocities and flow speeds across the Agadir Basin based on: (i) the shear velocity needed to suspend the coarsest observed sand grains; and (ii) the downslope gravitational driving force associated with flows of known thickness and layer-averaged sediment concentrations ranging between 0·5% and 9% volume. These calculations suggest that flows, especially in the proximal parts of the basin, were powerful enough to have eroded exposed sea floor mud. This may indicate that the flows were depositional from the moment they arrived at a given location, such that deposition by the flow shielded the underlying hemipelagic mud from erosion. Alternatively, key assumptions made during analysis for this study may be incorrect. For instance, sediment settling from high-concentration layers at the base of the flow may have been hindered, enabling flows to suspend their sediment loads at lower shear velocities. Reproducing the key field observations outlined here will be a challenge for future experimental and numerical models of submarine flows.

ACKNOWLEDGEMENTS

REFERENCES

Abad, J.D., **Sequeiros, O.E.**, **Spinewine, B.**, **Pirmez, C.**, **Garcia, M.H.** and **Parker, G.** (2011) Secondary current of saline underflow in a highly meandering channel: experiments and theory. *J. Sed. Res.*, **81**, 787–813.

Aberle, J., Nikora, V. and Walters, R. (2004) Effects of bed material properties on cohesive sediment erosion. *Mar. Geol.*, **207**, 83–93.

Allen, J.R.L. (1977) The possible mechanics of convolute lamination in graded sand beds. *J. Geol. Soc. London*, **134**, 19–31.

Allen, J.R.L. (1982) *Sedimentary Structures: Their Character and Physical Basis*, Vol. 1. Elsevier, Amsterdam.

Amos, C.L., Umgiesser, G., Ferrarin, C., Thompson, C.E.L., Whitehouse, R.J.S., Sutherland, T.F. and Bergamasco, A. (2010) The erosion rates of cohesive sediments in Venice lagoon, Italy. *Cont. Shelf Res.*, **30**, 859–870.

Amy, L.A. and Talling, P.J. (2006) Anatomy of turbidites and linked debrites based on long distance (120 x 30 km) bed correlation, Marnoso Arenacea Formation, Northern Apennines, Italy. *Sedimentology*, **53**, 161–212.

Arnott, R.W.C. (2012) Turbidites, and the case of the missing dunes. *J. Sed. Res.*, **82**, 379–384.

Baas, J.H., Best, J.L. and Peakall, J. (2011) Depositional processes, bedform development and hybrid bed formation in rapidly decelerated cohesive (mud-sand) sediment flows. *Sedimentology*, **58**, 1953–1987.

Bagnold, R.A. (1966) An approach to the sediment transport problem from general physics. Professional Paper of the U.S. Geological Survey 422-I.

Best, J. and Bridge, J. (1992) The morphology and dynamics of low amplitude bedwaves upon upper stage plane beds and the preservation of planar laminae. *Sedimentology*, **39**, 737–752.

Bouma, A.H. (1962) *Sedimentology of Some Flysch Deposits: A Graphic Approach to Facies Interpretation*. Elsevier, Amsterdam/New York, 168 pp.

Bowen, A.J., Normark, W.R. and Piper, D.J.W. (1984) Modelling of turbidity currents on Navy Submarine Fan, California Continental Borderland. *Sedimentology*, **31**, 169–185.

Brommer, M.B., Weltje, G.J. and Trincardi, F. (2009) Reconstruction of sediment supply from mass accumulation rates in the Northern Adriatic Basin (Italy) over the past 19,000 years. *J. Geophys. Res. (Earth Surf.)*, **114**, F02008. doi: 10.1029/2008jf000987.

Carter, L., Milliman, J.D., Talling, P.J., Gavey, R. and Wynn, R.B. (2012) Near-synchronous and delayed initiation of long run-out submarine sediment flows from a record-breaking river flood, offshore Taiwan. *Geophys. Res. Lett.*, **39**, 5.

Cattaneo, A., Babonneau, N., Ratzov, G., Dan-Unterseh, G., Yelles, K., Bracene, R., de Lepinay, B.M., Boudiaf, A. and Deverchere, J. (2012) Searching for the seafloor signature of the 21 May 2003 BoumerdSs earthquake offshore central Algeria. *Nat. Hazards Earth Syst. Sci.*, **12**, 2159–2172.

Cooper, C., Wood, J. and Andrieux, O. (2013) Turbidity Current Measurements in the Congo Canyon. Offshore Technology Conference, Houston, Texas, 6–9 May, Extended Abstracts.

Crowley, T.J. (1983) Depth dependent carbonate dissolution changes in the eastern North-Atlantic during the last 170, 000 years. *Mar. Geol.*, **54**, M25–M31.

Darby, S.E. and Peakall, J. (2012) Modelling the equilibrium bed topography of submarine meanders that exhibit reversed secondary flows. *Geomorphology*, **163**, 99–109.

Davies, T.L., VanNiel, B., Kidd, R.B. and Weaver, P.P.E. (1997) High-resolution stratigraphy and turbidite processes in the Seine Abyssal Plain, northwest Africa. *Geo-Mar. Lett.*, **17**, 147–153.

Dorrell, R.M., Darby, S.E., Peakall, J., Sumner, E.J., Parsons, D.R. and Wynn, R.B. (2013) Superelevation and overspill control secondary flow dynamics in submarine channels. *J. Geophys. Res. (Oceans)*, **118**, 3895–3915.

Duitt, T.H., Calder, E.S., Cole, P.D., Hoblitt, R.P., Loughlin, S.C., Norton, G.E., Ritchie, L.J., Sparks, R.S.J. and Voight, B. (2002) Small-volume, highly mobile pyroclastic flows formed by rapid sedimentation from pyrclastic surges at Soufriere Hills Volcano, Monserrat: an important volcanic hazard. In: *The Eruption of Soufriere Hills Volcano, Monserrat, From 1995 to 1999* (Eds T.H. Druitt and B.P. Kokelaar), *Geol. Soc. Mem.*, **21**, 263–279.

Eggenhuisen, J.T. and McCaffrey, W.D. (2012) The vertical turbulence structure of experimental turbidity currents encountering basal obstructions: implications for vertical suspended sediment distribution in non-equilibrium currents. *Sedimentology*, **59**, 1101–1120.

Frenz, M., Wynn, R.B., Georgiopoulou, A., Bender, V.B., Hough, G., Masson, D.G., Talling, P.J. and Cronin, B.T. (2008) Provenance and pathways of late Quaternary turbidites in the deep-water Agadir Basin, northwest African margin. *Int. J. Earth Sci.*, **98**, 721–733.

Garcia, M. and Parker, G. (1993) Experiments on the entrainment of sediment into suspension by a dense bottom current. *J. Geophys. Res. (Oceans)*, **98**, 4793–4807.

Gladstone, C. and Sparks, R.S.J. (2002) The significance of grain size breaks in turbidites and pyroclastic density current deposits. *J. Sed. Res.*, **72**, 182–191.

Grabowski, R.C., Droppo, I.G. and Wharton, G. (2011) Erodibility of cohesive sediment: the importance of sediment properties. *Earth Sci. Rev.*, **105**, 101–120.

Halka, J., Panageotou, W. and Sanford, L. (1991) Consolidation and erosion of deposited cohesive sediments in Northern Chesapeake Bay, USA. *Geo-Mar. Lett.*, **11**, 174–178.

Haughton, P., Davis, C., McCaffrey, W. and Barker, S. (2009) Hybrid sediment gravity flow deposits - Classification, origin and significance. *Mar. Petrol. Geol.*, **26**, 1900–1918.

Heezen, B.C., Menzies, R.J., Schneider, E.D., Ewing, W.M. and Granelli, N.C.L. (1964) Congo submarine canyon. *AAPG Bull.*, **48**, 1126–1149.

Hiscott, R.N. (1994) Loss of capacity, not competence, as the fundamental process governing deposition from turbidity currents. *J. Sed. Res. (A Sediment. Petrol. Process.)*, **64**, 209–214.

Hiscott, R.N., Hall, F.R. and Pirmez, C. (1997) Turbidity current overspill from the Amazon Channel: texture of the silt/sand load, paleoflow from anisotropy of magnetic susceptibility and implications for flow processes. In: *Proceedings of the Ocean Drilling Program Scientific Results*, Vol. 155. (Eds R.D. Flood, D.J.W. Piper, A. Klaus and L.C. Peterson), pp. 53–78. Ocean Drilling Program, College Station, TX.

Hsu, S.K., Kuo, J., Lo, C.L., Tsai, C.H., Doo, W.B., Ku, C.Y. and Sibuet, J.C. (2008) Turbidity currents, submarine landslides and the 2006 Pingtung earthquake off SW Taiwan. *Terr. Atmos. Oceanic Sci.*, **19**, 767–772.

Hughes Clarke, J.E. (1988) The geological record of the 1929 Grand Banks earthquake and its relevance to deep-sea clastic sedimentation. PhD Thesis, Dalhousie University, Halifax, Nova Scotia.

Hughes Clarke, J.E., Brucker, S., Muggah, J., Hamilton, T., Cartwright, D., Church, I. and Kuus, P. (2012) Temporal

progression and spatial extent of mass wasting events on the Squamish prodelta slope. 11th International Symposium on Landslides, Conference Proceedings, Banff, June 2012.

Clarke, J.H., Marques, C.V. and Pratomo, D. (2014) Imaging active mass-wasting and sediment flows on a fjord delta, Squamish, British Columbia. In: *Submarine Mass Movements and Their Consequences*, VI (Eds. S. Krastel, J.-H. Behrmann, D. Völker, M. Stipp, C. Berndt, R. Urgeles, J. Chaytor, K. Huhn, M. Strasser and C.B. Harbitz), *Adv. Nat.Technol. Hazards Res.*, 37, 249–260. Springer International Publishing.

Hunt, J.E., Wynn, R.B., Masson, D.G., Talling, P.J. and Teagle, D.A.H. (2011) Sedimentological and geochemical evidence for multistage failure of volcanic island landslides: a case study from Icod landslide on north Tenerife, Canary Islands. *Geochem. Geophys. Geosyst.*, 12, 1–36.

Jones, K.P.N., McCave, I.N. and Weaver, P.P.E. (1992) Textural and dispersal patterns of thick mud turbidites from the Madeira Abyssal Plain. *Mar. Geol.*, 107, 149–173.

Khripounoff, A., Vangriesheim, A., Babonneau, N., Crassous, P., Dennielou, B. and Savoye, B. (2003) Direct observation of intense turbidity current activity in the Zaire submarine valley at 4000 m water depth. *Mar. Geol.*, 194, 151–158.

Khripounoff, A., Vangriesheim, A., Crassous, P. and Etoubleau, J. (2009) High frequency of sediment gravity flow events in the Var submarine canyon (Mediterranean Sea). *Mar. Geol.*, 263, 1–6.

Khripounoff, A., Crassous, P., Lo Bue, N., Dennielou, B. and Jacinto, R.S. (2012) Different types of sediment gravity flows detected in the Var submarine canyon (northwestern Mediterranean Sea). *Prog. Oceanogr.*, 106, 138–153.

Klaucke, I., Hesse, R. and Ryan, W.B.F. (1997) Flow parameters of turbidity currents in a low-sinuosity giant deep-sea channel. *Sedimentology*, 44, 1093–1102.

Kneller, B. (2003) The influence of flow parameters on turbidite slope channel architecture. *Mar. Petrol. Geol.*, 20, 901–910.

Kneller, B.C. and Branney, M.J. (1995) Sustained high-density turbity currents and the deposition of thick massive sands. *Sedimentology*, 42, 607–616.

Kneller, B. and Buckee, C. (2000) The structure and fluid mechanics of turbidity currents: a review of some recent studies and their geological implications. *Sedimentology*, 47, 62–94.

Kneller, B.C. and McCaffrey, W.D. (1999) Depositional effects of flow non-uniformity and stratification within turbidity currents approaching a bounding slope: deflection, reflection and facies variation. *J. Sed. Res.*, 69, 980–991.

Kneller, B.C. and McCaffrey, W.D. (2003) The interpretation of vertical sequences in turbidite beds: the influence of longitudinal flow structure. *J. Sed. Res.*, 73, 706–713.

Kneller, B.C., Bennett, S.J. and McCaffrey, W.D. (1999) Velocity structure, turbulence and fluid stresses in experimental gravity currents. *J. Geophys. Res. (Oceans)*, 104, 5381–5391.

Komar, P.D. (1969) Channelized flow of turbidity currents with application to monterey deep-sea fan channel. *J. Geophys. Res.*, 74, 4544–4553.

Komar, P.D. (1971) Hydraulic jumps in turbidity currents. *Geol. Soc. Am. Bull.*, 82, 1477–1488.

Komar, P.D. (1973) Continuity of turbidity current flow and systematic variations in deep-sea channel morphology. *Geol. Soc. Am. Bull.*, 84, 3329–3334.

Komar, P.D. (1985) The hydraulic interpretation of turbidites from their grain sizes and sedimentary structures. *Sedimentology*, 32, 395–407.

Krause, D.C., White, W.C., Piper, D.J.W. and Heezen, B.C. (1970) Turbidity currents and cable breaks in Western New-Britain-Trench. *Geol. Soc. Am. Bull.*, 81, 2153–2160.

Kuenen, P.H. and Sengupta, S. (1970) Experimental marine suspension currents, competency and capacity. *Geol. Mijnbouw*, 49, 89–118.

Leeder, M.R. (1999) *Sedimentology: process and product.* George Allen and Unwin, London. pp 65–66.

Liu, J.T., Wang, Y.H., Yang, R.J., Hsu, R.T., Kao, S.J., Lin, H.L. and Kuo, F.H. (2012) Cyclone-induced hyperpycnal turbidity currents in a submarine canyon. *J. Geophys. Res. (Oceans)*, 117, C04033.

Lowe, D.R. (1982) Sediment gravity flows.2. Depositional models with special reference to the deposits of high-density turbidity currents. *J. Sed. Petrol.*, 52, 279–298.

Macdonald, H.A., Wynn, R.B., Huvenne, V.A.I., Peakall, J., Masson, D.G., Weaver, P.P.E. and McPhail, S.D. (2011) New insights into the morphology, fill, and remarkable longevity (>0.2 m.y.) of modern deep-water erosional scours along the northeast Atlantic margin. *Geosphere*, 7, 845–867.

McCave, I.N. and Jones, K.P.N. (1988) Deposition of ungraded muds from high-density non-turbulent turbidity currents. *Nature*, 333, 250–252.

Migeon, S., Mulder, T., Savoye, B. and Sage, F. (2012) Hydrodynamic processes, velocity structure and stratification in natural turbidity currents: results inferred from field data in the Var Turbidite System. *Sed. Geol.*, 245, 48–62.

Miller, M.C., McCave, I.N. and Komar, P.D. (1977) Threshold of sediment motion under unidirectional currents. *Sedimentology*, 24, 507–527.

Mitchener, H. and Torfs, H. (1996) Erosion of mud/sand mixtures. *Coast. Eng.*, 29, 1–25.

Nino, Y., Lopez, F. and Garcia, M. (2003) Threshold for particle entrainment into suspension. *Sedimentology*, 50, 247–263.

Normark, W.R., Paull, C.K., Caress, D.W., Ussler, W. and Sliter, R. (2009) Fine-scale relief related to Late Holocene channel shifting within the floor of the upper Redondo Fan, offshore Southern California. *Sedimentology*, 56, 1690–1704.

Ockenden, M.C. and Delo, E.A. (1988) Consolidation and erosion of estuarine mud and sand mixtures – an experimental study. HR Wallingford, Report No. SR 149.

Parchure, T.M. and Mehta, A.J. (1985) Erosion of soft cohesive sediment deposits. *J. Hydraul. Eng.*, 111, 1308–1326.

Parker, G., Garcia, M., Fukushima, Y. and Yu, W. (1987) Experiments on turbidity currents over an erodible bed. *J. Hydraul. Res.*, 25, 123–147.

Paull, C.K., Mitts, P., Ussler, W., Keaten, R. and Greene, H.G. (2005) Trail of sand in upper Monterey Canyon: Offshore California. *Geol. Soc. Am. Bull.*, 117, 1134–1145.

Peakall, J., Felix, M., McCaffrey, B. and Kneller, B. (2001) Particulate gravity currents: perspectives. In: *Particulate Gravity Currents* (Eds W. McCaffrey, B. Kneller and J. Peakall), *Int. Assoc. Sedimentol. Spec. Publ.*, 31, 1–8.

Pearce, T.J. and Jarvis, I. (1992) Composition and provenance of turbidite sands - Late Quaternary, Madeira Abyssal Plain. *Mar. Geol.*, 109, 21–51.

Piper, D.J.W. (1972) Turbidite origin of some laminated mudstones. *Geol. Mag.*, 109, 115–126.

Piper, D.J.W. (1978) Turbidite muds and silts on deepsea fans and abyssal plains. In: *Sedimentation in Submarine Canyons, Fans and Trenches* (Eds D.J. Stanley and G. Kelling), pp. 163–176. Dowden, Hutchinson and Ross, Stroudsburg, PA.

Piper, D.J.W., **Cochonat, P.** and **Morrison, M.L.** (1999) The sequence of events around the epicentre of the 1929 Grand Banks earthquake: initiation of debris flows and turbidity current inferred from sidescan sonar. *Sedimentology*, **46**, 79–97.

Pirmez, C. and **Imran, J.** (2003) Reconstruction of turbidity currents in Amazon Channel. *Mar. Petrol. Geol.*, **20**, 823–849.

Prior, D.B., **Bornhold, B.D.**, **Wiseman, W.J.** and **Lowe, D.R.** (1987) Turbidity current activity in a British Columbia Fjord. *Science*, **237**, 1330–1333.

Quaresma, V.D., **Amos, C.L.** and **Flindt, M.** (2004) The influences of biological activity and consolidation time on laboratory cohesive beds. *J. Sed. Res.*, **74**, 184–190.

Reynolds, S. (1987) A recent turbidity current event, Hueneme Fan, Califonia - Reconstruction of flow properties. *Sedimentology*, **34**, 129–137.

Rothwell, R.G., **Pearce, T.J.** and **Weaver, P.P.E.** (1992) Late Quaternary evolution of the Madeira Abyssal Plain, Canary Basin, NE Atlantic. *Basin Res.*, **4**, 103–131.

Sequeiros, O.E. (2012) Estimating turbidity current conditions from channel morphology: a Froude number approach. *J. Geophys. Res. (Oceans)*, **117**, C04003.

Soulsby, R. (1997) *The Dynamics of Marine Sands: A Manual for Practical Applications.* Thomas Telford Publications, London.

Stevenson, C.J., **Talling, P.J.**, **Wynn, R.B.**, **Masson, D.G.**, **Hunt, J.E.**, **Frenz, M.**, **Akhmetzhanhov, A.** and **Cronin, B.T.** (2013) The flows that left no trace: very large-volume turbidity currents that bypassed sediment through submarine channels without eroding the sea floor. *Mar. Petrol. Geol.*, **41**, 186–205.

Stevenson, C.J., **Talling, P.J.**, **Masson, D.G.**, **Sumner, E.J.**, **Frenz, M.** and **Wynn, R.B.** (2014) The spatial and temporal distribution of grain-size breaks in turbidites. *Sedimentology.* doi: 10.1111/sed.12091

Stow, D.A.V. and **Bowen, A.J.** (1978) Origin of lamination in deep-sea, fine-grained sediments. *Nature*, **274**, 324–328.

Stow, D.A.V. and **Bowen, A.J.** (1980) A physical model for the transport and sorting of fine-grained sediment by turbidity currents. *Sedimentology*, **27**, 31–46.

Stow, D.A.V. and **Mayall, M.** (2000) Deep-water sedimentary systems: new models for the 21st century. *Mar. Petrol. Geol.*, **17**, 125–135.

Stow, D.A.V. and **Piper, D.J.W.** (1984) Deep-water fine-grained sediments: facies models. In: *Fine-Grained Sediments: Deep-Water Processes and Facies* (Eds D.A.V. Stow and D.J.W. Piper), *Geol. Soc.*, **15**, 611–646.

Stow, D.A. and **Shanmugam, G.** (1980) Sequence of structures in fine-grained turbidites: comparison of recent deep-sea and ancient flysch sediments. *Sed. Geol.*, **25**, 23–42.

Straub, K.M. and **Mohrig, D.** (2008) Quantifying the morphology and growth of levees in aggrading submarine channels. *J. Geophys. Res. (Earth Surf.)*, **113**, 20.

Sumner, E.J., **Amy, L.A.** and **Talling, P.J.** (2008) Deposit structure and processes of sand deposition from decelerating sediment suspensions. *J. Sed. Res.*, **78**, 529–547.

Sumner, E.J., **Talling, P.J.**, **Amy, L.A.**, **Wynn, R.B.**, **Stevenson, C.J.** and **Frenz, M.** (2012) Facies architecture of individual basin-plain turbidites: comparison with existing models and implications for flow processes. *Sedimentology*, **59**, 1850–1887.

Talling, P.J. (2013) Hybrid submarine flows comprising turbidity current and cohesive debris flow: deposits, theoretical and experimental analyses, and generalized models. *Geosphere*, **9**, 460–488.

Talling, P.J., **Amy, L.A.** and **Wynn, R.B.** (2007a) New insight into the evolution of large-volume turbidity currents: comparison of turbidite shape and previous modelling results. *Sedimentology*, **54**, 737–769.

Talling, P.J., **Wynn, R.B.**, **Masson, D.G.**, **Frenz, M.**, **Cronin, B.T.**, **Schiebel, R.**, **Akhmetzhanov, A.M.**, **Dallmeier-Tiessen, S.**, **Benetti, S.**, **Weaver, P.P.E.**, **Georgiopoulou, A.**, **Zuhlsdorff, C.** and **Amy, L.A.** (2007b) Onset of submarine debris flow deposition far from original giant landslide. *Nature*, **450**, 541–544.

Talling, P.J., **Masson, D.G.**, **Sumner, E.J.** and **Malgesini, G.** (2012) Subaqueous sediment density flows: depositional processes and deposit types. *Sedimentology*, **59**, 1937–2003.

Talling, P.J., **Paull, C.K.** and **Piper, D.J.W.** (2014) How are subaqueous sediment density flows triggered, what is their internal structure and how does it evolve? Direct observations from monitoring of active flows. *Earth-Sci. Rev.*, **125**, 244–287.

van Tassell, J. (1981) Silver Abyssal-Plain carbonate turbidite – Flow characteristics. *J. Geol.*, **89**, 317–333.

van Tassell, J. (1986) The hydraulic interpretation of turbidites from their grain sizes and sedimentary structures. *Sedimentology*, **33**, 437–438.

Thompson, C.E.L., **Amos, C.L.**, **Angelaki, M.**, **Jones, T.E.R.** and **Binks, C.E.** (2006) An evaluation of bed shear stress under turbid flows. *J. Geophys. Res. (Oceans)*, **111**, C04008.

Tolhurst, T.J., **Black, K.S.**, **Shayler, S.A.**, **Mather, S.**, **Black, I.**, **Baker, K.** and **Paterson, D.M.** (1999) Measuring the in situ erosion shear stress of intertidal sediments with the Cohesive Strength Meter (CSM). *Estuar. Coast. Shelf Sci.*, **49**, 281–294.

Tolhurst, T.J., **Riethmuller, R.** and **Paterson, D.M.** (2000) In situ versus laboratory analysis of sediment stability from intertidal mudflats. *Cont. Shelf Res.*, **20**, 1317–1334.

Underwood, M.B. (1991) Submarine canyons, unconfined turbidity currents, and sedimentary bypassing of fore-arc regions. *Rev. Aquat. Sci.*, **4**, 149–200.

Vangriesheim, A., **Khripounoff, A.** and **Crassous, P.** (2009) Turbidity events observed in situ along the Congo submarine channel. *Deep Sea Res. (II Top. Stud. Oceanogr.)*, **56**, 2208–2222.

Vrolijik, P.J. and **Southard, J.B.** (1997) Experiments on rapid deposition of sand from high-velocity flows. *Geosci. Can.*, **24**, 45–54.

Weaver, P.P.E. (1991) Quaternary high-resolution stratigraphy and its application in studies of the Canary Basin. *AAPG Bull.*, **75**, 1424–1424.

Weaver, P.P.E. (1994) Determination of turbidity current erosional characteristics from reworked coccolith assemblages, Canary Basinm northeast Atlantic. *Sedimentology*, **41**, 1025–1038.

Weaver, P.P.E. and **Kuijpers, A.** (1983) Climatic control of turbidite deposition on the Madeira Abyssal Plain. *Nature*, **306**, 360–363.

Weaver, P.P.E. and **Rothwell, R.G.** (1987) Sedimentation on the Madeira Abyssal Plain over the last 300,000 years. In: *Geology and Geochemistry of Abyssal Plains* (Eds P.P.E.

Weaver and J. Thomson), *Geol. Soc. Spec. Publ.*, **31**, 71–86.

Weaver, P.P.E. and Thomson, J. (1993) Calculating erosion by deep-sea turbidity currents during initiation and flow. *Nature*, **364**, 136–138.

Weaver, P.P.E., Rothwell, R.G., Ebbing, J., Gunn, D. and Hunter, P.M. (1992) Correlation, frequency of emplacement and source directions of megaturbidites on the Madeira Abyssal Plain. *Mar. Geol.*, **109**, 1–20.

Whitehouse, R., Soulsby, R., Roberts, W. and Mitchener, H. (2000) *Dynamics of Estuarine Muds.* HR Wallingford and Thomas Telford, London, 210 pp.

Wynn, R.B., Kenyon, N.H., Masson, D.G., Stow, D.A.V. and Weaver, P.P.E. (2002a) Characterization and recognition of deep-water channel-lobe transition zones. *AAPG Bull.*, **86**, 1441–1462.

Wynn, R.B., Weaver, P.P.E., Masson, D.G. and Stow, D.A.V. (2002b) Turbidite depositional architecture across three interconnected deep-water basins on the north-west African margin. *Sedimentology*, **49**, 669–695.

Wynn, R.B., Talling, P.J., Masson, D.G., Stevenson, C.J., Cronin, B.T. and Le Bas, T.P. (2010) Investigating the timing, processes and deposits of one of the world's largest submarine gravity flows: the 'bed 5 event' off Northwest Africa. In: *Submarine Mass Movements and Their Consequences* (Eds D.C. Mosher, R.C. Shipp, L. Moscardelli, J.D. Chaytor, C.D.P. Baxter, H.J. Lee and R. Urgeles), *Adv. Nat. Technol. Hazards Res.*, **28**, 463–474.

Wynn, R.B., Talling, P.J., Masson, D.G., Le Bas, T.P., Cronin, B.T. and Stevenson, C.J. (2012) The influence of subtle gradient changes on deep-water gravity flows: a case study from the Moroccan Turbidite system. Application of the principles of seismic geomorphology to continental-slope and base-of-slope systems: case studies from seafloor and near seafloor analogues. *SEPM Spec. Publ.*, **99**, 371–383.

Xu, J.P., Noble, M.A. and Rosenfeld, L.K. (2004) In-situ measurements of velocity structure within turbidity currents. *Geophys. Res. Lett.*, **31**, 4.

Xu, J.P., Swarzenski, P.W., Noble, M. and Li, A.C. (2010) Event-driven sediment flux in Hueneme and Mugu submarine canyons, southern California. *Mar. Geol.*, **269**, 74–88.

Zakeri, A. (2008) A potentially devastating offshore geohazard - submarine debris flow impact on piplines. *Explor. Prod. Oil Gas Rev.*, **6**, 118–121.

Zeng, J.J., Lowe, D.R., Prior, D.B., Wiseman, W.J. and Bornhold, B.D. (1991) Flow properties of turbidity currents in Bute Inlet, British Columbia. *Sedimentology*, **38**, 975–996.

Supporting Information

Additional Supporting Information may be found in the online version of this article:

Figure S1. Transect 1 showing the turbidite stratigraphy along the axis of the Agadir Basin (Fig. 1; adapted from Talling *et al.* (2007b) and Frenz *et al.* (2008). Positions of cross-cutting transects 2 and 3 are marked (black circles). Cores are hung off sea floor topography (*ca* 650 times vertical exaggeration). Turbidites are shaded with colour whilst intervening hemipelagic sediment is white. Turbidites are labelled A1 to A14 (after Wynn *et al.*, 2002b). Average gradient is highlighted along the transect (dashed red lines). Beds A3, A5, A7, A11 and A12 are the focus of this study.

Figure S2. Transect 2 showing the turbidite stratigraphy from NW to SE across the north-eastern part of the Agadir Basin (Figure 1). Cores are hung off sea floor topography (*ca* 110 times vertical exaggeration). Position of cross-cutting transect 1 is marked (black circle). Turbidites are shaded with colour whilst intervening hemipelagic sediment is white. Turbidites are labelled A1 to A14 (Wynn *et al.*, 2002b). Beds A3, A5, A7, A11 and A12 are the focus of this study.

Figure S3. Transect 3 showing the turbidite stratigraphy from NW to SE across the south-western part of the Agadir Basin (Fig. 1). Cores are hung off sea floor topography (*ca* 110 times vertical exaggeration). Position of cross-cutting transect 1 is marked (black circle). Turbidites are shaded with colour whilst intervening hemipelagic sediment is white. Turbidites are labelled A1 to A14 (Wynn *et al.*, 2002b). Beds A3, A5, A7, A11 and A12 are the focus of this study. Intervals of poor core recovery are marked with a cross. Note interval of detailed analysis in core 26, where Bed A5 pinches out.

Figure S4. Effects of differential turbidite deposition on sea floor gradient across the Agadir Basin. Graph illustrates the calculated slopes along the axis of the Agadir Basin after sequential removal of Beds A3, A5, A7, A11 and A12 from the stratigraphy. Note that most of the beds do not alter the slope profile along the axis of the Agadir Basin. Collectively, the largest difference in slope generated by differential deposition across the basin is *ca* 0·007. Such small differences are probably within the error of the GEBCO data, and are considered insignificant.

Figure S5. Graph illustrating the density of hemipelagic sediments within the top 10 cm of cores collected from the Agadir Basin (see Fig. 1B for core locations). Density was obtained from a GEOTEK multi-sensor core logger. Dashed black lines denote the range of values used to calculate sea floor erosion thresholds.

Figure S6. These figures show detailed vertical grain-size profiles through deposits of Bed A3. Name of the bed and core numbers are labelled (see Fig. 1B for core locations). Each deposit is illustrated from left to right with a core photograph, interpretation of sedimentary structures (see Table 1 for facies codes), visual log and grain-size profiles (D_{10}, D_{50}, D_{90} and sorting values) (see Fig. 2 for key).

Figures S7 and S8. These diagrams show detailed vertical grain-size profiles through deposits of Bed A5. Name of the bed and core numbers are labelled (see Fig. 1B for core locations). Each deposit is illustrated from left to right with a core photograph, interpretation of sedimentary structures (see Table 1 for

facies codes), visual log and grain-size profiles (D_{10}, D_{50}, D_{90} and sorting values) (see Fig. 2 for key).

Figures S9 and S10. These diagrams show detailed vertical grain-size profiles through deposits of Bed A7. Name of the bed and core numbers are labelled (see Fig. 1B for core locations). Each deposit is illustrated from left to right with a core photograph, interpretation of sedimentary structures (see Table 1 for facies codes), visual log and grain-size profiles (D_{10}, D_{50}, D_{90} and sorting values) (see Fig. 2 for key).

Figures S11 and S12. These diagrams show detailed vertical grain-size profiles through deposits of Bed A11. Name of the bed and core numbers are labelled

(see Fig. 1B for core locations). Each deposit is illustrated from left to right with a core photograph, interpretation of sedimentary structures (see Table 1 for facies codes), visual log and grain-size profiles (D_{10}, D_{50}, D_{90} and sorting values) (see Fig. 2 for key).

Figures S13 and S14. These diagrams show detailed vertical grain-size profiles through deposits of Bed A12. Name of the bed and core numbers are labelled (see Fig. 1B for core locations). Each deposit is illustrated from left to right with a core photograph, interpretation of sedimentary structures (see Table 1 for facies codes), visual log and grain-size profiles (D_{10}, D_{50}, D_{90} and sorting values) (see Fig. 2 for key).